Characterizing Lithospheric Transverse Isotropy using Moment Tensors
- On the origin of the Non-double Couple Components of GCMT solutions -

Hitoshi Kawakatsu[1,2] (e-mail: hitosi@eri.u-tokyo.ac.jp)

[1]Earthquake Research Institute, The University of Tokyo, Japan
[2]Institute of Earth Sciences, Academia Sinica, Taiwan

Key Points

(1) Non-double couple components (NDCs) of GCMT can be due to lithospheric transverse isotropy (VTI)
(2) A method to invert for the lithospheric VTI using moment tensors is developed and applied to GCMT data
(3) Lithospheric VTI of PREM at sub-Moho explains observed NDC pattern but some adjustments may be necessary

Abstract

The seismic moment tensor, which represents the equivalent body-force system of the seismic source, may exhibit non-double couple components (NDCs) when the earthquake occurs on a planer fault if the source medium is anisotropic. Kawakatsu (1991a) reported that the NDCs of the moment tensors for shallow earthquakes from the Harvard CMT catalog exhibited a systematic characteristic dependent on faulting types: the sign of the NDC parameter ϵ on average systematically changes for thrust (negative), normal (positive), and strike-slip (positive) faults. The behavior of thrust and normal faults that shows opposite sign can be explained if the source region is transversely isotropic with a vertical symmetry axis (VTI, radially anisotropic). In fact, the VTI model of PREM at a sub-Moho depth predicts the observed systematic NDC pattern, although the magnitude is underestimated, indicating the potential to enhance our understanding of the lithospheric transverse isotropy using the NDC of the moment tensors. To investigate the lithospheric transverse isotropy structure utilizing the NDCs of the moment tensors, we propose a novel inversion scheme, building upon the approaches employed previously for deep and intermediate-depth earthquakes, but with necessary modifications to address shallow sources. Synthetic tests conducted under conditions of random faulting indicate the potential to constrain the S-wave anisotropy ξ and the fifth parameter η_κ, but with moderate to severe correlation depending on data types. The application of this method to real data sourced from the GCMT catalog suggests that the lithospheric transverse isotropy of PREM at the sub-Moho depth serves as a suitable initial model. However, some adjustments may be necessary, particularly regarding the fifth parameter, to enhance the model's fidelity in representing observed NDCs of the moment tensors. Finally, the behavior of the strike-slip faults that cannot be explained by the VTI may deserve further attention.

1 Introduction

The seismic moment tensor, which represents the equivalent body-force system of the seismic source (Backus and Mulcahy, 1976), may exhibit non-double couple components (NDCs) when an earthquake as a shear-faulting on a plane occurs in an anisotropic medium. Aki and Richards (1980), in their text book on seismology, states this as in the caption of Figure 3.7 as *"The nine possible couples that are required to obtain equivalent forces for a generally oriented displacement discontinuity in anisotropic media"*. As the Earth is elastically anisotropic (e.g., Babuska and Cara, 1991; Montagner and Mainprice, 2024), the moment tensor corresponding to an earthquake as faulting should naturally exhibits non-double couple components.

The era of broadband digital seismology started around the second half of 1970's has brought seismic moment tensor solutions of global moderate size earthquakes ($Mw \geq\sim 5.5$) available soon after their occurrence to the seismological community (e.g., Dziewonski et al., 1981; Sipkin, 1986; Kawakatsu, 1995). Using the early solutions of the Harvard Centroid Moment Tensor (HCMT) catalog, Giardini (1983, 1984) showed that the NDCs of the CMT solutions show systematic behavior for deep and inter-mediate depth earthquakes that might be related to the dominant stress pattern in the subducting slabs hosting those earthquakes. This view was followed by Kuge and Kawakatsu (1990, 1992, 1993) who showed that for events with large NDCs, the presence of multiple ruptures sharing a common dominant stress in earthquakes could explain the waveform complexity. More recently, for deep and intermediate-depth earthquakes, NDCs with relatively mild magnitudes, their origin due to seismic anisotropy have been discussed (Vavrycuk, 2004; Li et al., 2018); further, some theoretical aspects of the effect of anisotropy on the NDCs as forward (Menke and Russell, 2020) and inverse (Menke, 2020) problems have been introduced.

As for shallow earthquakes, while the global average properties show no systematic pattern, Kawakatsu (1991a) reported that the NDCs of the Harvard CMT catalog (Dziewonski et al., 1981) exhibited a systematic characteristic dependent on faulting types, which can be seen in more recent GCMT catalogue (Figure 1). The average NDC parameter ϵ (Giardini, 1983) is negative for thrust faulting (TF) and positive for normal faulting (NF) and strike-slip faulting (SS). While concluding that this systematic behavior cannot be explained by un-modeled random error in the inversion process, Kawakatsu (1991a) listed potential causes, such as the presence of multiple sub-events with different focal mechanisms sharing similar principal axes, near-source anisotropy, and the presence of systematic regional heterogeneities; although he preferred the first one, because it explains the nature of the NDCs occurring in the ridge-transform-fault plate boundaries, but left it as an open question. Further, Kuge and Lay (1994b) discussed the effect of the fault zone irregularity that might result in the systematic NDCs, and Kuge and Lay (1994a) showed the data-type dependence of the CMT inversion that might bias the size dependence of the NDCs.

The purpose of the present paper is to show that a part of the reported behavior related to thrust (TF) and normal (NF) faults by Kawakatsu (1991a) can be explained if the source region is transversely isotropic with a vertical symmetry axis (VTI, radially anisotropic) as in the reference earth model PREM (Dziewonski et al., 1981). We further investigate the potential to enhance our understanding of the lithospheric transverse isotropy using the NDC of the moment tensors. It should be noted that VTI here represents an averaged property of the lithospheric anisotropy that can be more complicated. As far as the lithospheric anisotropy originates from the causes that share similar characteristics, as an (azimuthal) average property, VTI emerges as in PREM. In this regard, we first discuss the global feature of the NDCs that may be modeled with VTI. Then, as a natural extension of the approach, we model the difference between ocean and continent and discuss the future research perspectives.

2 Non-double couple components and transverse isotropy (VTI)

2.1 Non-double couple components of the moment tensor

The seismic moment tensor $\boldsymbol{M}$, which is the point source representation of the indigenous seismic source of the stress-glut distribution (Backus and Mulcahy, 1976), is a 3×3 symmetric tensor; it has six degrees of freedom and can be characterized by three eigen-solutions. For an earthquake of a shear dislocation on a planar fault, it can be expressed as,

$$M_{pq} \;=\; u_i \nu_j C_{ijpq}, \tag{1}$$

where u_i and ν_j respectively correspond to the shear displacement integrated on the fault plane and the unit normal vector to the fault plane, and C_{ijpq} to the elastic tensor of the the source region (Aki and Richards, 1980). For the case of an isotropic source region, it is reduced to

$$M_{pq} \;=\; \mu \left(u_p \nu_q + u_q \nu_p\right) \tag{2}$$

that represents the double-couple source with four degrees of freedom with the constraints,

$$trace(\boldsymbol{M}) = 0, \tag{3}$$

which is equivalent to the orthonormality between the slip vector and the fault normal,

$$\boldsymbol{u} \cdot \boldsymbol{\nu} = 0, \tag{4}$$

and

$$\lambda_2 \;=\; 0 \;\; (\lambda_1 + \lambda_3 = 0) \tag{5}$$

where $\lambda_1 \geq \lambda_2 \geq \lambda_3$ are the eigenvalues of $\boldsymbol{M}$.

The two extra degrees of freedom of a general moment tensor are called non-double couple components (NDCs), and their strength can be measured by the isotropic component

$$I \;=\; \frac{1}{3} trace(\boldsymbol{M}) \tag{6}$$

and the intermediate eigenvalue λ_2 both scaled by the seismic moment. Due to the difficulty of constraining the isotropic component, most of the global catalogues, such as those provided by [H,G]CMT, USGS, etc, assume $I = 0$ to report zero-trace (deviatoric) moment tensors. The strength of the deviatoric NDC is often measured by

$$\epsilon \;=\; \frac{-\lambda_2}{max(|\lambda_1|,\, |\lambda_3|)} \tag{7}$$

(Giardini, 1983). For a deviatoric moment tensor,

$$\epsilon \;=\; \frac{1}{2} C_{CLVD} \tag{8}$$

where C_{CLVD} is define by Vavrycuk (2015) in the "standard decomposition".

In the standard decomposition, a moment tensor $\boldsymbol{M}$, after the diagonalization, is decomposed into three base (unit) tensors corresponding to the isotropic (ISO), the double-couple (DC), and the compensated linear vector dipole (CLVD) types; base tensors are defined such that the largest magnitude of eigenvalues is equal to one. Then, the corresponding "components", M_{ISO}, M_{DC}, and M_{CLVD}, are defined by

$$\begin{aligned} M_{ISO} &= \frac{1}{3}(\lambda_1 + \lambda_2 + \lambda_3) && (9) \\ M_{DC} &= \frac{1}{2}(\lambda_1 - \lambda_3 - |\lambda_1 + \lambda_3 - 2\lambda_2|) && (10) \\ M_{CLVD} &= \frac{2}{3}(\lambda_1 + \lambda_3 - 2\lambda_2), && (11) \end{aligned}$$

where M_{DC} is always positive, and other NDC components do not have the restriction. The total seismic moment M is given by

$$M = |M_{ISO}| + M_{DC} + |M_{CLVD}|, \quad (12)$$

to scale the fractional strength of each component, C_{ISO}, C_{DC}, C_{CLVD} to make $|C_{ISO}| + C_{DC} + |C_{CLVD}| = 1$.

2.2 Lithospheric transverse isotropy (VTI) and NDCs

The reference earth model PREM (Dziewonski and Anderson, 1981) has a layer with transverse isotropy with a vertical symmetry axis (VTI) in a depth range of 24.4km - 220km that may correspond to the lithosphere-asthenosphere system where the shear deformation due to the plate motion may dominate. While VTI S-wave and P-wave parameters (i.e., $\beta_{[V,H]}$ and $\alpha_{[V,H]}$) should be well (relatively speaking) constrained with $\beta_H > \beta_V$ and $\alpha_H > \alpha_V$, whether or not the fifth parameter η_κ introduced by Kawakatsu (2016a) is constrained is uncertain (see Table 1 and Figure S1).

We characterize the lithospheric VTI using the five parameters, $\beta_{[V,H]}, \alpha_{[V,H]}, \eta_\kappa$, following Kawakatsu (2016a). As for a characteristic value of VTI, we choose the sub-Moho parameters at a depth of 24.4km where the fifth parameter η_κ shows the smallest value (Table 1). Figure 2 shows the distribution of NDCs expected for earthquakes occurring in a source region with VTI of sub-Moho PREM. One thousand faults with random orientations are generated (Figure 2a), and resulting NDCs are plotted on a diagram introduced by Vavrycuk (2015) (Figure 2b) that is essentially the same as the $\tau - k$ plot originally developed by Hudson et al. (1989) except for the sign of the horizontal (C_{CLVD}) axis. Different faulting types are classified with colors (red: thrust fault (TF); green: normal fault (NF); blue strike skip (SS); yellow: the rest). While blue points (SS) are evenly distributed near around the origin, which represents the pure-DC moment tensor, green (NF) and red (TF) points are located respectively on the positive and negative side of C_{CLVD} values. This faulting type dependence of the NDC parameter (ϵ or C_{CLVD}) for normal and thrust faults is what is observed by Kawakatsu (1991a, Figure 1). Considering that PREM is the reference earth model, it seems reasonable (or natural) to infer that the reported systematic NDC distribution is due to the presence of VTI in the lithosphere. The average values reported by Kawakatsu (1991a) are $\bar{\epsilon} = 0.049 \pm 0.005$ for NF and $\bar{\epsilon} = -0.055 \pm 0.003$ for TF (the numbers after $\pm$ here represent standard errors for the mean estimates). The corresponding values for the synthetic modeling shown in Figure 2 are $\bar{C}_{CLVD} = \pm 0.079 \pm 0.012$, and considering their mutual relationship in equation (8), the magnitudes (absolute) modeled by PREM are smaller than those of the data. This indicates a potential to used NDCs of observed (or reported) moment tensor solutions to further constrain the lithospheric transverse anisotropy.

Although the points in Figure 2b appear to be linearly scattered and the isotropic component (C_{ISO}) is generally weak, this is not always the case. Figure 3 shows how changing the VTI parameters affects the NDC distribution, where we fix both S ($\xi = \frac{\beta_H^2}{\beta_V^2}$) and P($\phi^{-1} = \frac{\alpha_H^2}{\alpha_V^2}$) anisotropy to the PREM values and vary the fifth parameter η_κ. With the constant strength of P- and S-anisotropy (i.e., ξ and ϕ^{-1}), it can be seen that the strength of NDCs varies significantly. For example, the spread of C_{CLVD} for a case $\eta_\kappa = 1.10$ (Figure 3f) is more than three times compared to the PREM case (i.e., $\eta_\kappa = 0.97$, Figure 3c). Similarly, Figure 4 shows the case of varying ξ while fixing others to sub-Moho PREM. It is worthwhile to note that the decrease of ξ rotates the NDC pattern counter-clockwise, and when $\xi = 1.00$ (Figure 4a) and $\xi = 0.95$ (Figure 4f), the polarity of ϵ reverses. Therefore, $\xi > 1.00$, i.e., $\beta_H > \beta_V$, is required for the lithospheric VTI from the distribution of NDCs of moment tensors. The behavior of NDCs further supports the idea of using NDCs to constrain the VTI parameters of the source region (similar figures showing the ϕ^{-1} effects and corresponding *r0-projection* are provided in the Supplemental Material (Figures S3,S4,S5,S6)).

3 Characterization of lithospheric VTI via NDC of Moment Tensors: Method

Vavrycuk (2004) first introduced a general methodology to invert for the source region anisotropy using the NDCs of moment tensors of deep earthquakes in the Tonga subduction zone, and later Li et al. (2018) applied the methodology to solve for tilted transverse anisotropy (TTI) in the subducting slabs. We propose a novel inversion scheme, building upon the approaches employed by them, but with necessary modifications to address shallow sources (Kawakatsu, 1996).

3.1 Inversion for full moment tensors

Following Vavrycuk (2004), we rewrite equation (1) using the Voigt notation (in bold lowercase),

$$\boldsymbol{m} \;=\; \boldsymbol{c}\boldsymbol{d}, \tag{13}$$

where $\boldsymbol{c}$ is a 6×6 matrix of the elastic coefficients in the Voigt notation, $\boldsymbol{m}$ and $\boldsymbol{d}$ are six elements vectors defined as

$$\boldsymbol{m} \;=\; (M_{11}, M_{22}, M_{33}, M_{23}, M_{13}, M_{12})^T, \tag{14}$$

and

$$\boldsymbol{d} \;=\; (u_1\nu_1, u_2\nu_2, u_3\nu_3, u_2\nu_3 + u_3\nu_2, u_1\nu_3 + u_3\nu_1, u_1\nu_2 + u_2\nu_1)^T. \tag{15}$$

The vector $\boldsymbol{d}$ is closely related to the symmetric dyadic source tensor, $\boldsymbol{D} = (u_p\nu_q + u_q\nu_p)/2$, and

$$\boldsymbol{D} \;=\; \frac{1}{2}\begin{pmatrix} 2d_1 & d_6 & d_5 \\ d_6 & 2d_2 & d_4 \\ d_5 & d_4 & 2d_3 \end{pmatrix} \tag{16}$$

(Vavrycuk, 2005, see also equation (2)). (Note that neither $\boldsymbol{D}$ nor $\boldsymbol{d}$ here is scaled as in Vavrycuk (2005) due to our definition of $\boldsymbol{u}$.)

Our goal is to find a set of elastic coefficients $\boldsymbol{c}$ for a given set of scaled moment tensor solutions $\tilde{\boldsymbol{m}}_i$ $(i = 1, .., n)$ that share a common anisotropic source structure, such that some cost (or misfit) function as

$$\Gamma_m = \frac{1}{n} \sum ||\tilde{\boldsymbol{m}}_i - \boldsymbol{c}\hat{\boldsymbol{d}}_i||^2, \tag{17}$$

can be minimized with a constraint requiring $\hat{\boldsymbol{D}}_i$ to represent a double-couple source tensor (i.e., trace=0 with the zero intermediate eigenvalue), where $||\cdot||$ represents the Frobenius norm of a matrix. This approach makes sense in the ordinary least-squares way, but leads to a two-step process that consists of (1) for each $\tilde{\boldsymbol{m}}_i$, finding $\hat{\boldsymbol{d}}_i$, for a given $\boldsymbol{c}$, that minimizes the squared difference in (17), and (2) then look for $\boldsymbol{c}$ that minimizes the summation of the squared differences, that requires some computing cost.

An alternative approach suggested by Vavrycuk (2004) is to directly solve for

$$\hat{\boldsymbol{d}}_i = \boldsymbol{c}^{-1}\tilde{\boldsymbol{m}}_i \tag{18}$$

for each $\tilde{\boldsymbol{m}}_i$ to minimize a cost function

$$\sum |Trace(\hat{\boldsymbol{D}}_i) + Det(\hat{\boldsymbol{D}}_i)|, \tag{19}$$

where $\hat{\boldsymbol{D}}_i$ denotes the source tensor corresponding to $\hat{\boldsymbol{d}}_i$ but not necessarily represents the double couple. This approach offers a quick way to get to a solution but the meaning of cost function might not be obvious. Besides, the determinant is a highly nonlinear function of the elements that may introduce many local minimums for the cost function when its summation is used. The $Trace(\boldsymbol{D}) = 0$ constraint can be incorporated as a linear constraint, $d_1 + d_2 + d_3 = 0$, in the least-squares inverse, thus we use an alternative measure for the cost function that is given in the next section.

3.2 Inversion for Zero-Trace moment tensors

3.2.1 Projection of the isotropic component

Because of the difficulty of constraining certain components of the moment tensor particularly for shallow sources (e.g., Kanamori and Given, 1981; Kawakatsu, 1996), the trace of moment tensor solutions of the catalogues, such as GCMT (Dziewonski et al., 1981; Ekstrom, 2012), USGS, W-phase (Kanamori and Rivera, 2008), are constrained to be zero.

It is important to note that this Zero-Trace moment tensor ($\boldsymbol{M}^*$) is not the same as the deviatoric part of the true moment tensor ($\boldsymbol{M}^{Dev}$),

$$\boldsymbol{M}^* \neq \boldsymbol{M}^{Dev}. \tag{20}$$

By constraining $M^*_{11} + M^*_{22} + M^*_{33} = 0$ in moment tensor inversions, the isotropic component, which is present in the moment tensor in anisotropic medium, will be mapped into other components, most likely to the diagonal parts. Kawakatsu (1996) investigated the observability of the isotropic component in the CMT inversion of Dziewonski et al. (1981), and showed that, for shallow earthquakes, the isotropic component and the vertical CLVD components are strongly correlated and cannot be resolved separately (the correlation coefficients are -0.99 for surface wave data and -0.85 for the bodywave data). For deep earthquakes, the usage of various bodywave phases improve the situation that allows to constrain the isotropic part (Kawakatsu, 1991b, 1996). Therefore, instead of assuming $\boldsymbol{M}^* = \boldsymbol{M}^{Dev}$

as done in the previous work (Vavrycuk, 2004; Li et al., 2018), we need to think that the reported Zero-Trace MT is a function (projection) of the original MT,

$$\boldsymbol{M}^* = \mathcal{F}(\boldsymbol{M}). \tag{21}$$

Assuming the azimuthal station coverage is reasonably good, which may be satisfied for global moderate size earthquakes (say $Mw \geq 5.5$), we assume that the isotropic component I will be converted equally to the two horizontal diagonal components; i.e.,

$$\begin{aligned} M_{11}^* &= M_{11} + \beta \times I \\ M_{22}^* &= M_{22} + \beta \times I \\ M_{33}^* &= M_{33} + \alpha \times I, \end{aligned} \tag{22}$$

where subscripts 1 and 2 represent the horizontal components, and subscript 3 denotes the vertical component in Cartesian coordinates. The ratio of mapping coefficients $r = \alpha/\beta$ defines how the mapping is done; summing both sides, $\alpha = -3r/(r+2)$ and $\beta = -3/(r+2)$ are derived. For the case of previous researches, $r = 1$ and $\alpha = \beta = -1\cancel{/3}$ (*r1-projection*) are presumed. In our case for shallow earthquakes, the result of Kawakatsu (1996) indicates that the long-period surface wave excitation due to the isotropic moment tensor $\boldsymbol{I} = [1, 1, 1]$ and the vertical CLVD MT $\boldsymbol{C} = [0.5, 0.5, -1]$, where numbers in parentheses represent the diagonal components of the moment tensor with the rest components being zero, are nearly equal in magnitude and opposite in sign (*cf.* Table 1 and Figure 2 of Kawakatsu (1996) and references therein), and thus indistinguishable; so, M_I will be converted to M_C as $M_C = -M_I$ that requires $r = 0$ and $\alpha = 0$, $\beta = -1.5$ (*r0-projection*), resulting

$$\begin{aligned} M_{11}^* &= M_{11} - 1.5I \\ M_{22}^* &= M_{22} - 1.5I \\ M_{33}^* &= M_{33}. \end{aligned} \tag{23}$$

We do not expect this to occur for each earthquake exactly, but for a large number of earthquakes, on the average, we suggest this provides a likely expectation. It should be also noted that, strictly speaking, the condition $r = 0$ does not apply for the case of the long-period bodywaves that still show the strong negative correlation of the resolvability between $\boldsymbol{I}$ and $\boldsymbol{C}$. Considering that the CMT methodology relies on both datasets, r may be considered as an adjustable parameter (close to 0), but here we assume $r = 0$ for shallow earthquakes for the rest of analysis.

3.2.2 The misfit function

As discussed by Vavrycuk (2004), for a catalogue Zero-Trace MT solution

$$\boldsymbol{m^*} = (M_{11}^*, M_{22}^*, M_{33}^*, M_{23}^*, M_{13}^*, M_{12}^*)^T, \tag{24}$$

the equation (13) needs to be modified. The introduction of *r-projection* requires

$$\boldsymbol{m^*} = \boldsymbol{bd} \tag{25}$$

where

$$
\begin{aligned}
b_{ij} &= c_{ij} + \beta \cdot \frac{c_{1j}+c_{2j}+c_{3j}}{3} \quad (i=1,2) \\
b_{ij} &= c_{ij} + \alpha \cdot \frac{c_{1j}+c_{2j}+c_{3j}}{3} \quad (i=3\ \ ) \\
b_{ij} &= c_{ij} \qquad\qquad\qquad\qquad (i=4-6).
\end{aligned}
\tag{26}
$$

Because $\boldsymbol{c}$ to $\boldsymbol{b}$ conversion is associated with a loss of degree of freedom due to *r-projection*, the matrix $\boldsymbol{b}$ is singular and does not have an inverse (this point is not well discussed in Vavrycuk (2004)). Here we can use the Zero-Trace property of $\boldsymbol{D}$ (i.e., $d_1+d_2+d_3=0$) as a constraint to solve

$$
\boldsymbol{d} \ = \ \boldsymbol{b}_{\boldsymbol{cg}}^{\boldsymbol{-1}} \boldsymbol{m}^{\boldsymbol{*}}, \tag{27}
$$

where $\boldsymbol{b}_{\boldsymbol{cg}}^{\boldsymbol{-1}}$ denotes the constrained generalized inverse of $\boldsymbol{b}$ (Li (2020); Jiaxuan Li (personal communication, 2023)). The resulting $\boldsymbol{d}$ and the associated source tensor $\boldsymbol{D}$ (instead of the moment tensor) have the Zero-Trace property, but the other required property for double-couple, i.e., the intermediate eigenvalue λ_2 to be zero may be unsatisfied. So for the misfit function, we use the "non-double couple" measure ϵ (equation (7)) of the source tensor $\boldsymbol{D}_i$ as

$$
\Gamma_{CLVD} \ = \ \frac{1}{n}\sum |C^{D_i}_{CLVD}|^2 \ = \ \frac{4}{n}\sum |\epsilon^{D_i}|^2, \tag{28}
$$

where $i = 1,..,n$ denotes i-th moment tensor solution. This measure of the misfit function shares similar characteristics to the least-squares type measure (17) such that the results may be compared with each other (Figure S2). In fact, it can be shown that each term in the summation of (28) (i.e., $|\epsilon^{D_i}|^2$) is equal to a half of the sum of the squared differences of the scaled eigenvalues of $\boldsymbol{D}_i$ (i.e., $[\lambda_1^{D_i}, \lambda_2^{D_i}, \lambda_3^{D_i}]/max(|\lambda_1^{D_i}|, |\lambda_3^{D_i}|)$) from the corresponding double-couple (i.e., $[1, 0, -1]$) sharing the same principal axes. This approach offers much faster way to estimate the minimum solution compared to (17). It may be noted that the natural extension of (28), i.e., $\Gamma_{NDC} = \sum(C^2_{CLVD} + C^2_{ISO})/n$, might be useful for the case when full moment tensor solutions are available.

4 Characterization of lithospheric VTI via NDC of Moment Tensors: Analysis

Our strategy is that we perform a series of grid-searches in the model parameter space of $\xi - \phi^{-1} - \eta_\kappa$ with a grid size of 0.01. As for the P-anisotropy parameter ϕ^{-1}, we parameterize it as a function of ξ as

$$
\phi^{-1} \ \sim \ \xi^{\alpha}, \tag{29}
$$

where α is the S-P scaling parameter. Before going into the analysis of real data, we first examine the resolution of VTI parameters from the NDCs of synthetic moment tensors. Then, as a first step toward characterizing the lithospheric anisotropy using NDCs of moment tensors, we apply the the developed methodology to the entire dataset of the GCMT catalogue to discuss future perspectives. We note that the term "lithospheric" here refers to regions where earthquakes occur and thus the inferences made will be limited to that sort of the lithosphere where earthquake activity is high.

4.1 Resolution analysis

Figure 5 shows the distribution of the misfit function (28) in $\eta_\kappa - \xi$ parameter space for a set of moment tensors synthesized (noise free) for 100 randomly oriented faulting (Kagan, 2005) in VTI medium with the PREM parameters at a depth of 24.4km (Table 1). Figure 5a shows the case when we scale P-anisotropy ϕ^{-1} to S-anisotropy ξ with that of the PREM value and indicates that the resolution is not uniform; i.e., there exits a moderate trade-off between η_κ and ξ. The situation can be more drastic when we restrict the faulting type (Figure 5c,d); if faulting is limited to a certain type only (TF, NF or SS), there occurs a strong trade-off between η_κ and ξ (or ϕ^{-1}). Since earthquakes occur under a regional stress field resulting in limited faulting types, this poses a limitation of the method, especially to the regional inference. Due to the symmetry of this inverse problem for TF and NF, for random faults, integrated effects of TF and ~~RF~~ in total overcomes the effect of SS resulting in the moderate trade-off seen in Figure 5a. Figure 5b shows the result similar to Figure 5a but with S-P scaling equals to one (i.e., $\phi^{-1} = \xi$). It should be noted that the minimum point shifts to lower(-left) relative to the input value (red asterisk).

4.2 Application to GCMT 1976-2023

We apply the methodology developed above to the entire dataset of the Global Centroid Moment Tensor (GCMT) catalogue (Ekstrom, 2012; Dziewonski et al., 1981) from a period of Jan., 1976 to Nov., 2023. We select shallow events depths above 50 km for $Mw \geq 5.5$. The magnitude control is partly to assure a good station azimuthal coverage. As to the further solution quality controls: we select solutions with (1) formal error estimates (both for location and MT-components) given, and (2) the MT-component relative error smaller than 0.08 (Vavrycuk, 2004). The first condition utilizes the flag information provided in the GCMT catalogue, and is to avoid poor station distribution and poor resolution of certain components. This condition limits event depth to be deeper than (or equal to) 10km. With these conditions employed, there are 9487 GCMT solutions left to be analyzed.

Figure 6 shows the result for three different S-P scaling cases. The first thing to notice is that there exits the strong negative tradeoff between η_κ and ξ as seen in the resolution test just for TF (or NF) type sources (Figure 5c). It seems likely that this reflects the fact that strike-skip type events generally show the distribution of NDCs negative (Figure 1c) without following the VTI prediction (see Discussion). Therefore, the resulting resolution figure reflects the resolution due to other two-type sources resulting in a strong trade-off. This means that, solely from the NDC distribution, it is difficult to constrain the VTI parameters (say, both ξ and η_κ at the same time). On the other hand, the situation can be improved using other data. For example, Kawakatsu (2016b) showed that Rayleigh wave phase velocities are sensitive to β_V and η_κ, but more sensitive to β_V than to η_κ (∼7:1 at a period of 30s where the sensitivities have peaks around a depth of 50 km, as indicated by the slope (converted for ξ) in Figures 6 as a reference). Therefore, by combing the NDC analysis with Rayleigh wave dispersion measurements, we may be able to constrain two parameters independently.

Secondly to notice is that the location of the minimum-valley shifts relative to the PREM value depicted by a red asterisk in each plot. It is likely that the points along the minimum valley are equally good candidates for a “solution” and there is weak resolution to distinguish the difference (Figure 7). For example, if the SP-scaling is known to be equal to that of PREM, it can be inferred that the PREM VTI parameters (at a depth of 24.4km) is generally consistent with the NDC distribution

(Figure 6b). However, the SP-scaling of PREM that is $\alpha =\sim 0.45$ is fairly small, and for the mantle rock olivine, the scale factor is somewhere between 1 and 1.5 (e.g., Kawakatsu, 2022). So, if we accept these values, then the results in Figure 6c,d may indicate that η_κ is smaller and ξ is slightly larger than the PREM values to be consistent with the NDCs.

5 Discussion

5.1 Error analysis

Figure 7 shows the result of 500 bootstrap resampling grid searches of the GCMT moment tensors. The strong tradeoff of parameters can be seen as a cloud of the minimum grid points scattered along the valley of the misfit function map. The formal Bootstrap estimates are $\xi = 1.108 \pm 0.022$ and $\eta_\kappa = 0.918 \pm 0.031$ with the correlation coefficient of $Cor = -0.99$. As discussed above, combining this with the tradeoff constraint given from Rayleigh wave dispersion measurements, we should have better estimates of VTI parameters. It should be noted that, in the case of PREM (Dziewonski et al., 1981), as various data sources are incorporated in the modeling, the trade-off situation could be significantly better for β_V than the simple Rayleigh wave prediction.

5.2 Ocean *vs* Continent

Considering the plate tectonic origin of the earthquake occurrence and the lithospheric structure, we may expect different VIT solutions for oceanic and continental areas. From the entire dataset, we classify events into ocean and continent respectively if the geographic altitude of the source location is below -2000 m or above 0 m. Figure 8 compares the analysis results, and the general trend (the location of the minimum valley to the PREM value) appears to be similar. Although the minimum points are farther away from the isotropic point ($\eta_\kappa = \xi = 1$) for the oceanic region than for the continental, the difference might be within the uncertainty (Figure 7). Nevertheless, it is interesting to note the observation that the apparent departure is stronger for the oceanic region. It is known that many of the rock-fabrics of the continental lithosphere (mostly crust) are anisotropic (Brownlee et al., 2017) and, when azimuthally averaged, VTI comparable to the oceanic fabrics may appear Kawakatsu (2021). The difference between continent and ocean in this regard is that the degree of the alignment of fabrics that may be stronger in the oceanic lithosphere than the continental one because of the simpler history of the development that may be seen here as the result of the ocean-continent regionalized analysis. Further regionalization and/or the plate-tectonic classification (ridge, subduction zone, transform fault, etc.) is possible, but then VTI may be too simple and it is better to be modeled by more general anisotropy that is beyond the scope of this paper.

5.3 Time Variation: the effects of data-type

From the moment tensor catalogue characteristic view, it may be of interest to see if there is any time dependence of the inversion results. Along the development history of the Harvard and Global CMT projects over the past 40 more years, the number of stations has been increasing and the methodological developments exist (Dziewonski et al., 1981; Ekstrom, 2012); so, we may expect some changes in the inversion result. According to Ekstrom (2012) there was a major development for the events after 2004. Figure 9(a),(b) compare the results before and after the change. There are two noticeable changes; one is the relative location of the minimum valley with respect to the PREM point. The other is the value of the minimum misfit (event average). The decrease of the misfit may indicate that the NDCs may be better determined after 2004, which might be also reflected in the nature of the inference for the VTI parameters. It appears that the corresponding full dataset result in Figure 6c indicates stronger influence of the recent (post 2004) result.

To understand the nature of this time variation, we investigate the impact of the data-type used for the CMT inversion (Kuge and Lay, 1994a). We further classify the data into those with bodywave only (B) and with bodywave and (mantle) surface wave combined (C) solutions using the data-type flag of the GCMT catalog (Ekstrom, 2012). The bodywave only solutions are for events till the end of 2003 (plus one on Feb. 24, 2004), and combined solutions span the whole period. Figure S7 compares the results for the events before the change (i.e., 1976-2003) for B and C data-types. Here again, the difference of the relative location of the minimum valley with respect to the PREM point is notable and appears even stronger. As noted in Section 3.2.1, the *r-projection* is expected to be different for the bodywave solution and the surface wave combined solution, the difference of Figure S7 (a) and (b) is likely due to the difference in the value of r for the corresponding datasets; the average ϵ values for thrust and normal faults are about twice as large (in absolute value) for bodywave only solution compared to those for combined solutions for events before 2004 (Table S1, Figure S7). Figure 9(c) shows the result for the entire period for the combined data-type that appears close to the result of the entire dataset within the model uncertainty (Figure 7). So, the inclusion of the bodywave only solutions to the entire dataset does not seem affecting the results significantly, but a further investigation might be worth making.

5.4 Spread of the NDC distribution: the effects of azimuthal anisotropy and 3D-structure

The VTI models discussed in this paper mainly concern the average property of the NDC distribution for the thrust faults and normal faults, but not the other statistical property, the spread (i.e., standard deviation) of the distribution. To delineate the effect of azimuthal anisotropy (in addition to VTI) on the NDC distribution, we generate synthtic faults with random orientations for hypothetical source regions that consist of well documented mantle fabrics (for the detail of modeling, see the caption of Table 2). Figure 10 and Table 2 compare those statistical properties. The VTI models generally explain the average but not the spread of the NDC distribution (Table 2: PREM and those with a superscript circle; Figure 10b); the predicted spread values are $0.01 - 0.02$ that are much less of what are seen in GCMT data (~ 0.2). On the other hand, the expected spreads for the randomly generated faultings for the mantle fabrics predict about 5 times larger spreads (Table 2, Figure 10c) that may account for 1/3 of the observed spread in GCMT solutions. This suggests a possibility that the significant portion of the observed (spread of) the GCMT NDCs are due to the seismic anisotropy of the lithosphere. Modeling of the effect the realistic azimuthal anisotropy (e.g., Schaeffer and Lebedev, 2013; Debayle et al., 2016; Becker et al., 2014) with the GCMT solutions may quantify to what extent the seismic anisotropy contribute the observed NDCs that is beyond the scope of the present paper.

In this account, the recent effort to incorporate the 3D-structural effect in the waveform modeling for the global CMT inversion (Hjorleifsdottir and Ekstrom, 2010; Sawade et al., 2022) is essential. Earlier, by inverting synthetic waveforms calculated for a 3D-structure with the GCMT methodology, Hjorleifsdottir and Ekstrom (2010) reports that *the error in the NDC is very small when using all wave-types to constrain the solution.* More recently, by conducting the CMT inversion using Green's functions computed by the spectral-element method in the 3-D model, Sawade et al. (2022) reports that *the overall distribution of source type* (meaning NDCs) *as a function of depth remains nearly unchanged.* As this is a still on-going active research (Sawade et al., 2023), it would be important to see how the final result after the full iteration modifies the distribution of the NDCs. It might be also important to understand how the Zero-Trace constraint modifies the *r-projection* in different inversion schemes.

Before closing this section, it should be also noted that the modeling of the VTI parameters conducted in this paper is not just for the average of ϵ values, but, as discussed in Sections 3 and 4, actually fitting individual moment tensors that have different source (fault) orientations.

5.5 On the fabric and Vs/Vp-anisotropy scaling

Kawakatsu (2021, 2022) summarizes the possible scaling relation between P- and S-anisotropy parameters, ξ and ϕ^{-1} as,

$$\phi^{-1} \sim \xi^{1.0-1.5}, \tag{30}$$

for various mantle fabrics. In the case of Russell et al. (2019), who constructed a model of 70-Ma oceanic lithosphere in Pacific based on the in-situ OBS measurements, the scaling value of 1.0 is employed. As for the oceanic sub-Moho azimuthal anisotropy, Shinohara et al. (2008) estimated the P-wave and S-wave variations to be about 5% and 3.5%, respectively, indicating that the P-wave anisotropy is larger than that of S-wave. All these appear to indicate that the scaling value for PREM at a depth of 24.4km (i.e., sub-Moho) is 0.43 is exceptionally small that reflects the general observation that P-wave anisotropy in PREM is fairly small.

Considering these, we suggest that the results in Figures 6c,d are more probable, indicating that η_κ and ξ are respectively slightly over- and under-estimated in PREM. The mantle fabrics show $\eta_\kappa \sim 0.98$ for $\xi \sim 1.10$ (Kawakatsu, 2022) that is larger than the $\eta_\kappa \sim 0.9685$ of PREM at 24.4km (Table 1). The presence of laminated scatterer observed in the both continental and oceanic lithosphere (e.g., Kennett and Furumura, 2016; Shito et al., 2013; Kennett and Furumura, 2015; Takeuchi et al., 2017) may further contribute to lower η_κ.

5.6 Enigma of strike-slip earthquakes

The VTI model employed in this paper, as a cause of the NDCs for TF and NF, cannot explain the those of strike slip events. Menke and Russell (2020), in their theoretical account, conclude that *both ISO and CLVD components are zero when the axis of symmetry is within the fault plane or the auxiliary plane.* As this is the case for VTI and a pure strike-slip fault, we expect zero or small NDCs for strike-slips. The positive shift of the average ϵ for SS events is strong and persistent, and it is unlikely that seismic azimuthal anisotropy explains it either as discussed by Kawakatsu (1991a). Instead, Kawakatsu (1991a) attributed the cause to the presence of multiple faultings in the ridge-transform-fault environment in the plate tectonics context (i.e., near simultaneous occurrence of strike-slip and normal faulting there), and suggested that it is related to that particular plate boundary related phenomenon. However, the positive shift of ϵ for SS events can be seen in the continental data, though the magnitude of the shift appears smaller (Table 2). In this view, it might be related to the some peculiar nature of strike-slip earthquakes that the current author cannot think of.

6 Concluding remarks

As the earth lithosphere is elastically anisotropic, the moment tensor of an earthquake as a planar faulting naturally exhibits non-double couple components including the isotropic component. The reported moment tensor catalogues often report only zero-trace moment tensors ($\boldsymbol{M}^*$) that are modified somehow to become deviatoric with $Trace(\boldsymbol{M}^*) = 0$ constraint in the inversion by possibly modifying the other moment tensor elements. In the present paper, we have attempted to show how this transformation (or projection) may be taking place for shallow earthquakes of the Harvard and Global Centroid Moment Tensor project catalogues. After confirming the presence of the systematic fault-type dependence of NDCs, which was reported earlier for the HCMT catalogue, in the modern GCMT catalogue, we have also shown how to retrieve useful parameters of the lithosphere, such as transverse isotropy structure, from the distribution of NDCs. The application of the methodology to the entire GCMT dataset indicates the PREM sub-Moho VTI model offers a suitable initial model. Whether or not the suggested further model adjustment is needed is uncertain, considering that the other processes, such as the simultaneous occurrence of multiple-faulting sharing similar dominant stress axes, might be also contributing to the systematic NDC behavior. Some of the findings of the exercise include (1) the systematic NDC pattern of thrust and normal faults indicates that $\xi > 1$ (i.e., $\beta_H > \beta_V$), for the shallow lithosphere (likely for oceanic), (2) the lithospheric azimuthal anisotropy should contribute the spread of the NDC pattern. Lastly, the enigmatic behavior of the NDCs of the strike-slip earthquakes seems to deserve further attention.

Data and Resources

The GCMT data analyzed in this paper are downloaded from the source in the public domain: [Global CMT Web Page, https://www.globalcmt.org/] on February 21, 2024. Most of computations and figures are made using the Matlab software. The Supplemental Material provides some introduction material for transverse isotropy with a vertical symmetry axis (VTI) and supplemental figures further facilitate the discussion of the main text.

Declaration of Competing Interests

The author declares no competing interests.

Acknowledgements

The author thanks Drs. Vaclav Vavrycuk, Yingcai Zheng, and Jiaxuan Li for the earlier discussion about their work. He is also grateful to the GCMT project for their excellent work making the quality CMT solutions available to the community. Comments by the reviewers helped to improve the manuscript. This study is partly supported by the KAKENHI Grant 22H01330 and 23K22601 from the Japan Society for the Promotion of Science (JSPS).

References

Aki, K., Richards, P., 1980. Quantitative Seismology: Theory and Methods. W. H. Freeman, New York.

Babuska, V., Cara, M., 1991. Seismic Anisotropy in the Earth. Kluwer Acad., Boston, Mass.

Backus, G., Mulcahy, M., 1976. Moment tensors and other phenomenological descriptions of seismic sources, I. Continuous displacements. Geophys. J. Roy. Astr. Soc. 46, 341–361.

Becker, T.W., Conrad, C.P., Schaeffer, A.J., Lebedev, S., 2014. Origin of azimuthal seismic anisotropy in oceanic plates and mantle. Earth Planet. Sci. Lett. 401, 236–250. doi:10.1016/j.epsl.2014.06.014.

Ben-Ismail, W., Mainprice, D., 1998. An olivine fabric database: An overview of upper mantle fabrics and seismic anisotropy. Tectonophysics 296, 145–157. doi:10.1016/S0040-1951(98)00141-3.

Brownlee, S.J., Schulte-Pelkum, V., Raju, A., Mahan, K., Condit, C., Orlandini, O.F., 2017. Characteristics of deep crustal seismic anisotropy from a compilation of rock elasticity tensors and their expression in receiver functions. Tectonics 36, 1835–1857. doi:10.1002/2017TC004625.

Debayle, E., Dubuffet, F., Durand, S., 2016. An automatically updated S-wave model of the upper mantle and the depth extent of azimuthal anisotropy. Geophys. Res. Lett. 43, 674–682. doi:10.1002/2015gl067329.

Dziewonski, A.M., Anderson, D.L., 1981. Preliminary reference Earth model. Phys. Earth Planet. In. 25, 297–356.

Dziewonski, A.M., Chou, T.A., Woodhouse, J.H., 1981. Determination of earthquake source parameters from waveform data for studies of global and regional seismicity. J. Geophys. Res. 86, 2825–2852.

Ekstrom, G., 2012. The global CMT project 2004-2010: Centroid-moment tensors for 13017 earthquakes. Phys. Earth Planet. In. 200-201, 1–9.

Giardini, D., 1983. Regional deviation of earthquake source mechanisms from the <<double-couple>> model, in *Earthquakes: observation, theory and interpretation (Kanamori, H., ed.).* pp. 345–353.

Giardini, D., 1984. Systematic analysis of deep seismicity: 200 centroid-moment tensor solutions for earthquakes between 1977 and 1980. Geophys. J. Roy. Astr. Soc. 77, 883–914.

Hjorleifsdottir, V., Ekstrom, G., 2010. Effects of three-dimensional Earth structure on CMT earthquake parameters. Phys. Earth Planet. In. 179, 178–190. doi:10.1016/j.pepi.2009.11.003.

Hudson, J.A., Pearce, R.G., Rogers, R.M., 1989. Source type plot for inversion of the moment tensor. J. Geophys. Res. 94, 765–774. doi:10.1029/ JB094iB01p00765.

Jung, H., Katayama, I., Jian, Z., Hiraga, T., Karato, S., 2006. Effect of water and stress on the lattice-preferred orientation of olivine. Tectonophysics 421, 1–22.

Kagan, Y.Y., 2005. Double-couple earthquake focal mechanism: random rotation and display. Geophys. J. Int. 163, 1065–1072. doi:10.1111/j.1365-246X.2005.02781.x.

Kanamori, H., Given, J., 1981. Use of long-period surface waves for rapid determination of earthquake source parameters. Phys. Earth Planet. In. 27, 8–31.

Kanamori, H., Rivera, L., 2008. Source inversion of W phase: speeding up seismic tsunami warning. Geophys. J. Int. 175, 222–238. doi:10.1111/j.1365-246X.2008.03887.x.

Kaverina, A.N., Lander, A.V., Prozorov, A.G., 1996. Global creepex distribution and its relation to earthquake-source geometry and tectonic origin. Geophys. J. Int. 125, 249–265.

Kawakatsu, H., 1991a. Enigma of earthquakes at ridge-transform-fault plate boundaries - distribution of non-double couple parameter of Harvard CMT solutions. Geophys. Res. Lett. 18, 1103–1106. doi:10.1029/91GL01238.

Kawakatsu, H., 1991b. Insignificant isotropic component in the moment tensor of deep earthquakes. Nature 351, 50–53. doi:10.1038/351050a0.

Kawakatsu, H., 1995. Automated near-realtime CMT inversion. Geophys. Res. Lett. 22, 2569–2572.

Kawakatsu, H., 1996. Observability of the isotropic component of a moment tensor. Geophys. J. Int. 126, 525–544. doi:10.1111/j.1365-246X.1996.tb05308.x.

Kawakatsu, H., 2016a. A new fifth parameter for transverse isotropy. Geophys. J. Int. 204, 682–685. doi:10.1093/gji/ggv479.

Kawakatsu, H., 2016b. A new fifth parameter for transverse isotropy II: partial derivatives. Geophys. J. Int. 206, 360–367. doi:10.1093/gji/ggw152.

Kawakatsu, H., 2021. Unexpected consequences of transverse isotropy. Bull. Seismol. Soc. Am. 111, 129–138. doi:10.1785/0120200205.

Kawakatsu, H., 2022. Erratum to Unexpected Consequences of Transverse Isotropy. Bull. Seismol. Soc. Am. 112, 1190–1190. doi:10.1785/0120210328.

Kennett, B.L.N., Furumura, T., 2015. Toward the reconciliation of seismological and petrological perspectives on oceanic lithosphere heterogeneity. Geochemistry Geophysics Geosystems 16, 3129–3141. doi:10.1002/ 2015GC006017.

Kennett, B.L.N., Furumura, T., 2016. Multiscale seismic heterogeneity in the continental lithosphere. Geochemistry Geophysics Geosystems 17, 1–19. doi:10.1002/ 2015GC006200.

Kuge, K., Kawakatsu, H., 1990. Analysis of a deep "non-double couple" earthquake using very broadband data. Geophys. Res. Lett. 17, 227–230.

Kuge, K., Kawakatsu, H., 1992. Deep and intermediate-depth non-double couple earthquakes: interpretation of moment tensor inversions using very broadband seismic waves. Geophys. J. Int. 111, 589–606.

Kuge, K., Kawakatsu, H., 1993. Significance of non-double couple components of deep and intermediate-depth earthquakes: implication from moment tensor inversions of various long-period seismic waves. Phys. Earth Planet. In. 75, 243–266.

Kuge, K., Lay, T., 1994a. Data-dependent non-double-couplecomponents of shallow earthquake sourceme chanisms: Effects of waveform inversion instability. Geophys. Res. Lett. 21, 9–12.

Kuge, K., Lay, T., 1994b. Systematic non-double-couple components of earthquake mechanisms: The role of fault zone irregularity. J. Geophys. Res. 99, 15457–15467.

Kustowski, B., Ekstrom, G., Dziewonski, A.M., 2008. Anisotropic shear-wave velocity structure of the Earth's mantle: A global model. Earth Planet. Sci. Lett. 113, B06306. doi:10.1029/2007JB005169.

Li, J., 2020. Inverting In-situ Anisotropy in Global Subduction Slabs Using Deep Earthquakes and Imaging Binary Mixtures and Fractures. Ph.D. Thesis, University of Houston.

Li, J., Zheng, Y., Thomsen, L., Lapen, T.J., Fang, X., 2018. Deep earthquakes in subducting slabs hosted in highly anisotropic rock fabric. Nature Geoscience 11, 696–700. doi:10.1038/s41561-018-0188-3.

Menke, W., 2020. Analytic Solution to the Moment Tensor - Anisotropy Inverse Problem. Pure Appl. Geophys. 177, 3119–3133. doi:10.1007/s00024-020-02468-2.

Menke, W., Russell, J.B., 2020. Non-Double-Couple Components of the Moment Tensor in a Transversely Isotropic Medium. Bull. Seismol. Soc. Am. 110, 1125–1133. doi:10.1785/0120190319.

Montagner, J.P., Mainprice, D., 2024. Anisotropic Seismology. Cambridge University Press, Cambridge.

Russell, J.B., Gaherty, J.B., Lin, P.Y.P., Lizarralde, D., Collins, J.A., Hirth, G., Evans, R.L., 2019. High-resolution constraints on Pacific upper mantle petrofabric inferred from surface-wave anisotropy. J. Geophys. Res. Solid Earth 124, 631–657. doi:10.1029/2018JB016598.

Russell, J.B., Gaherty, J.B., Mark, H.F., Hirth, G., Hansen, L.N., Lizarralde, D., Collins, J.A., Evans, R.L., 2022. Seismological Evidence for Girdled Olivine Lattice-Preferred Orientation in Oceanic Lithosphere and Implications for Mantle Deformation Processes During Seafloor Spreading. Geochemistry Geophysics Geosystems 23, e2022GC010542. doi:10.1029/2022GC010542.

Sawade, L., Beller, S., Lei, W., Tromp, J., 2022. Global centroid moment tensor solutions in a heterogeneous earth: the CMT3D catalogue. Geophys. J. Int. 231, 1727–1738. doi:10.1093/gji/ggac280.

Sawade, L., Ekstrom, G., Ding, L., Peter, D.B., Liu, Q., Nettles, M., Tromp, J., 2023. Global 3-D Centroid Moment Tensor Inversions Using Stored Global Green Functions From GLAD-M25. Abstract S23B-06 presented at AGU23, 11-15 Dec. .

Schaeffer, A.J., Lebedev, S., 2013. Global shear speed structure of the upper mantle and transition zone. Geophys. J. Int. 194, 417–449. doi:10.1093/gji/ggt095.

Shinohara, M., Fukano, T., Kanazawa, T., Araki, E., Suyehiro, K., Mochizuki, M., Nakahigashi, K., Yamada, T., Mochizuki, K., 2008. Upper mantle and crustal seismic structure beneath the northwestern Pacific basin using a seafloor borehole broadband seismometer and ocean bottom seismometers. Phys. Earth Planet. In. 170, 95–106.

Shito, A., Suetsugu, D., Furumura, T., Sugioka, H., Ito, A., 2013. Small-scale heterogeneities in the oceanic lithosphere inferred from guided waves. Geophys. Res. Lett. 40, 1708–1712. doi:10.1002/Grl.50330.

Sipkin, S.A., 1986. Estimation of earthquake source parameters by the inversion of waveform data; global seismicity, 1981-1983. Bull. Seismol. Soc. Am. 76, 1515–1541.

Takeuchi, N., Kawakatsu, H., Shiobara, H., Isse, T., Sugioka, H., Ito, A., Utada, H., 2017. Determination of intrinsic attenuation in the oceanic lithosphere-asthenosphere system. Science 358, 1593–1596. doi:10.1126/science.aao3508.

Vavrycuk, V., 2004. Inversion for anisotropy from non-double-couple components of moment tensors. J. Geophys. Res. 109, B07306. doi:10.1029/2003JB002926.

Vavrycuk, V., 2005. Focal mechanisms in anisotropic media. Geophys. J. Int. 161, 334–346. doi:10.1111/j.1365-246X.2005.02585.x.

Vavrycuk, V., 2015. Moment tensor decompositions revisited. J. Seismol. 19, 231–252. doi:10.1007/s10950-014-9463-y.

Depth km	Density g/ccm	α_V km/s	α_H km/s	β_V km/s	β_H km/s	η_κ	ξ	ϕ^{-1}
24.4	3.381	8.022	8.190	4.396	4.612	0.9685	1.101	1.042
60.0	3.377	7.982	8.165	4.404	4.580	0.9805	1.081	1.046
120	3.370	7.914	8.121	4.418	4.526	1.001	1.049	1.053
220	3.360	7.801	8.049	4.441	4.436	1.034	0.997	1.065

Table 1: PREM VTI model parameters for selected depths. Calculated using Love's coefficients of the 1 sec model.

Data source	Total number	Thrust			Normal			Strike slip		
		N	μ	σ	N	μ	σ	N	μ	σ
HCMT	5841	1732	-0.11	0.2*	858	0.098	0.29*	1318	0.070	0.2*
GCMT	12773	4848	-0.090	0.194	1537	0.076	0.275	3547	0.092	0.245
GCMT*	9487	3807	-0.092	0.180	1012	0.078	0.253	2810	0.094	0.235
GCMT$^\star_l$	1357	397	-0.102	0.229	158	0.086	0.302	390	0.065	0.306
GCMT$^\star_o$	5756	2278	-0.095	0.170	682	0.081	0.241	1990	0.105	0.212
GCMT$^\star_-$	4065	1603	-0.109	0.187	335	0.103	0.270	1197	0.075	0.244
GCMT$^\star_+$	5422	2204	-0.080	0.173	677	0.066	0.243	1613	0.108	0.228
GCMT$^\star_C$	6858	2742	-0.077	0.169	821	0.070	0.244	2021	0.097	0.232
PREM	10000	3285	-0.080	0.012	3286	0.080	0.012	3728	0.000	0.019
A-type	10000	3311	-0.065	0.062	3304	0.067	0.063	3437	0.001	0.046
A-type$^\circ$	10000	3264	-0.065	0.014	3261	0.067	0.014	3492	0.000	0.003
D-type	10000	3278	-0.127	0.079	3249	0.126	0.079	3866	0.000	0.029
D-type$^\circ$	10000	3214	-0.123	0.021	3234	0.124	0.021	3875	0.000	0.008
NoMelt	10000	3238	-0.074	0.067	3244	0.072	0.066	3709	0.000	0.023
NoMelt$^\circ$	10000	3202	-0.072	0.011	3262	0.072	0.011	3658	0.000	0.006

Table 2: Statistics of NDCs via $C_{CLVD}(= 2\epsilon)$. As to the data source, HCMT refers to the data used in Kawakatsu (1991a); GCMT to those in Section 4.2 with the quality control (1); GCMT* to those with the additional quality control (2) that is used for the analysis. Those below the first separation line are further grouped: subscripts l and o to continental and oceanic data used in Section 5.2; subscripts $-$ and $+$ to pre-2004 and post-2004 data used in Section 5.3; subscripts C to combined data-type (1976.01-2023.11) used in Section 5.3; note that most of post-2004 data correspond to combined data-type. Those below the second separation line are for synthetic data of 10000 randomly generated faults. C_{CLVD} values correspond to those estimated after the *r0-projection*. PREM refers to the sub-Moho PREM model; A-type to the A-type olivine of Jung et al. (2006); D-type to the D-type olivine of Ben-Ismail and Mainprice (1998); NoMelt to the model for the shallowest 70-Ma Pacific oceanic lithosphere from the direct OBS measurements Russell et al. (2022). For these fabrics, b-axis is assumed to be vertical. Superscript $^\circ$ indicates azimuthally averaged VTI model. * for certain σ indicates the standard deviation calculated from the standard error estimates given in the original paper (Kawakatsu, 1991a).

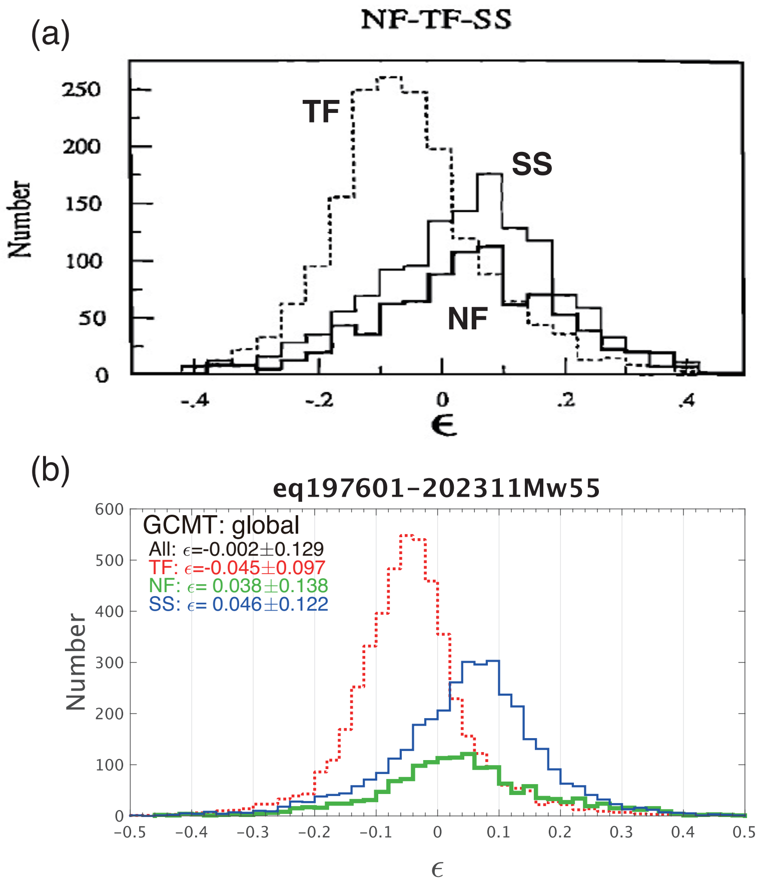

Figure 1: Distribution of the NDC parameter ϵ of shallow earthquakes for the Harvard (a) and the Global (b) CMT catalogues. (a) after Kawakatsu (1991a). The data consisted of 5481 shallow (<50km) earthquakes that occurred between Jan., 1977 and Sept., 1989 from the Harvard CMT catalogue. (b) 12773 shallow ($\leq$50km) earthquakes between Jan., 1976 and Nov., 2023 from the Global CMT catalogue ($M_w \geq$5.5; Table 2). The source type is classified by the angle (θ) of the principal axis (T, P, or B-axis) of moment tensors from the vertical axis (i.e., thrust (TF), normal (NF) and strike-slip (SS) faults are for θ_T, θ_P, and θ_B less than 30^o degrees, respectably).

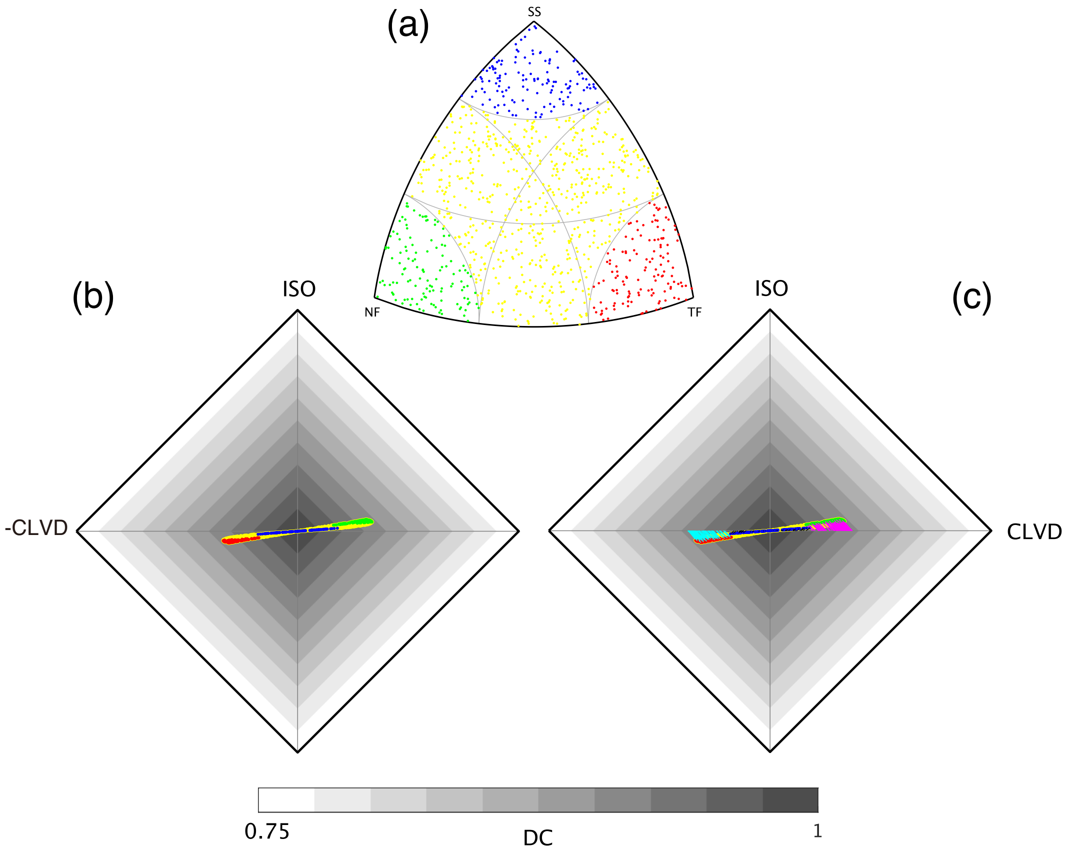

Figure 2: Simulation of 1000 random faults and the distribution of resulting NDCs due to the PREM sub-Moho VTI model. Fault-types are indicated by the color (red, green, and blue are for TF, ~~RF~~, and SS; yellow for the rest). (a) Distribution of 1000 faults plotted on the fault-type diagram (Kaverina et al., 1996; Kagan, 2005). (b) Distribution of the resulting NDCs plotted on the diamond CLVD-ISO diagram (Vavrycuk, 2015), where the horizontal and vertical axes denote the strength of CLVD and ISO-components, C_{CLVD} and C_{ISO}. (c) The same as (b), but paths of *r0-projection* lines are plotted by cyan, purple, and black lines for TF, NF, and SS. The shade-scale at the bottom indicates the strength of the DC-component. Note that (b) and (c) show only the central part of the whole diagram and that the origin corresponds to the pure DC source.

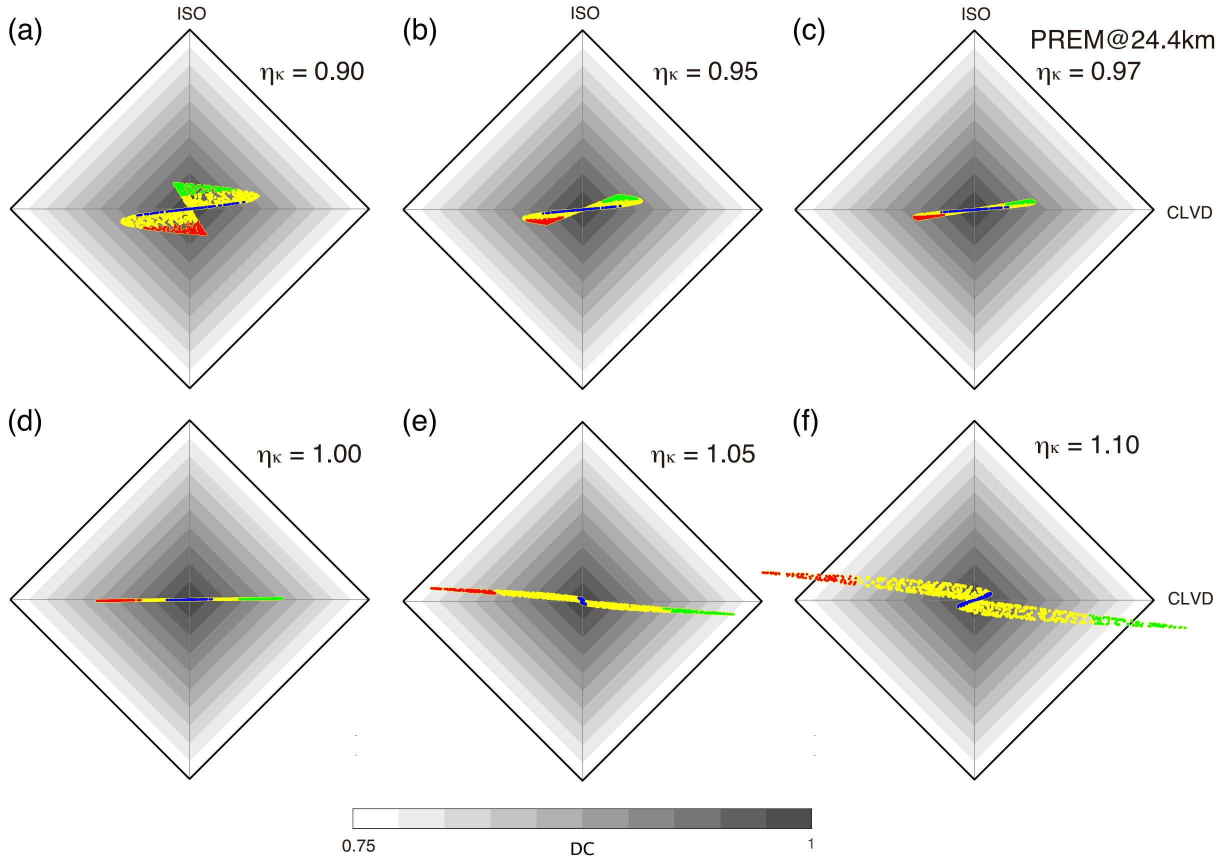

Figure 3: The same as Figure 2b, but for different VTI models with varying η_κ value: (a) η_κ=0.90, (b) 0.95, (c) PREM sub-Moho (0.97), (d) 1.00, (e) 1.05, (f) 1.10

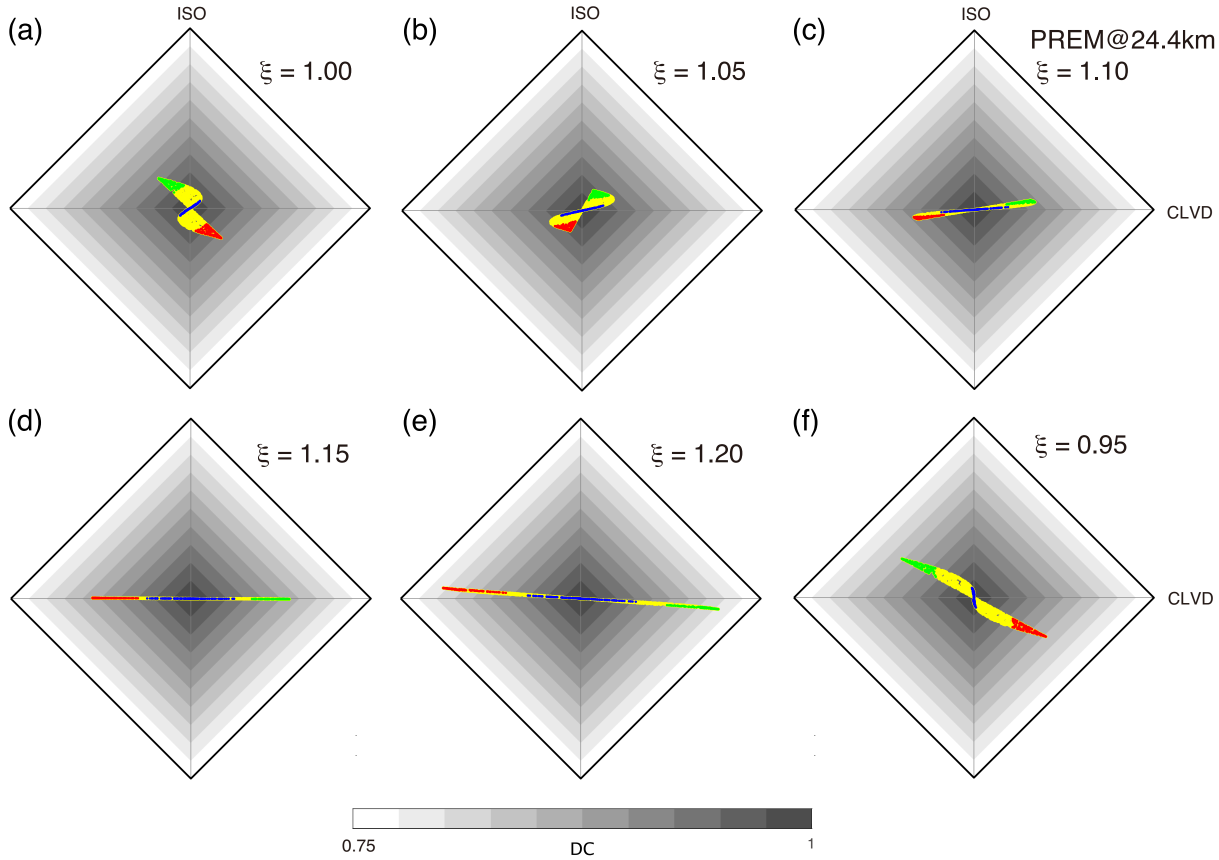

Figure 4: The same as Figure 2b, but for different VTI models with varying ξ value: (a) ξ=1.00, (b) 1.05, (c) PREM sub-Moho (1.10), (d) 1.15, (e) 1.20, (f) 0.95. Similar figures for varying ϕ^{-1} is in Figure S3.

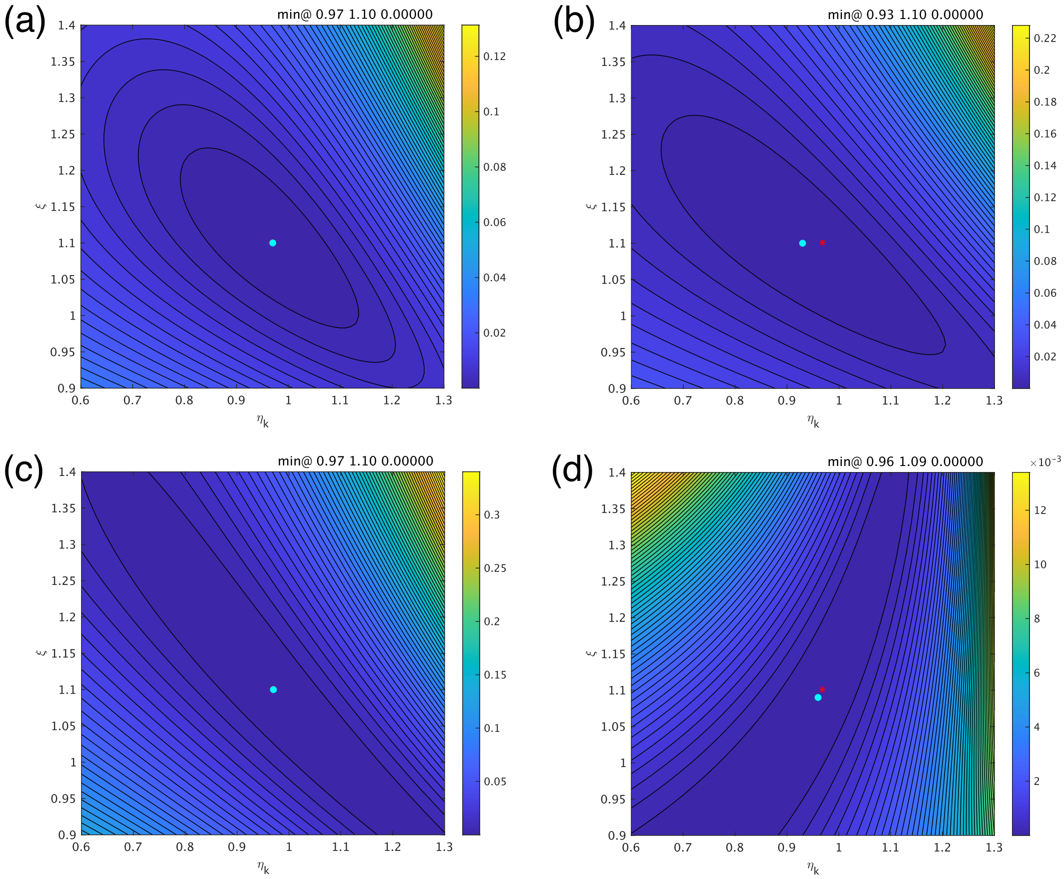

Figure 5: The resolution of the model VTI parameters in $\eta_\kappa - \xi$ domain. The point in cyan color gives the minimum const-function location, and the red asterisk denotes the PREM sub-Moho point as a reference. (a) 100 random faults are used as the input MT-data, (b) the same as (a), but S-P scaling 1.0 is employed, (c) 100 random thrust faults (TF) are used (a similar result occurs for ~~RF~~ data due to the symmetry of the problem), (d) 100 random strike-slip faults (SS) are used. The same S-P scaling as that of PREM sub-Moho is employed for (a), (c), and (d). The three digits at the top in each figure give the minimum point (η_κ, ξ) and the corresponding misfit value in (28).

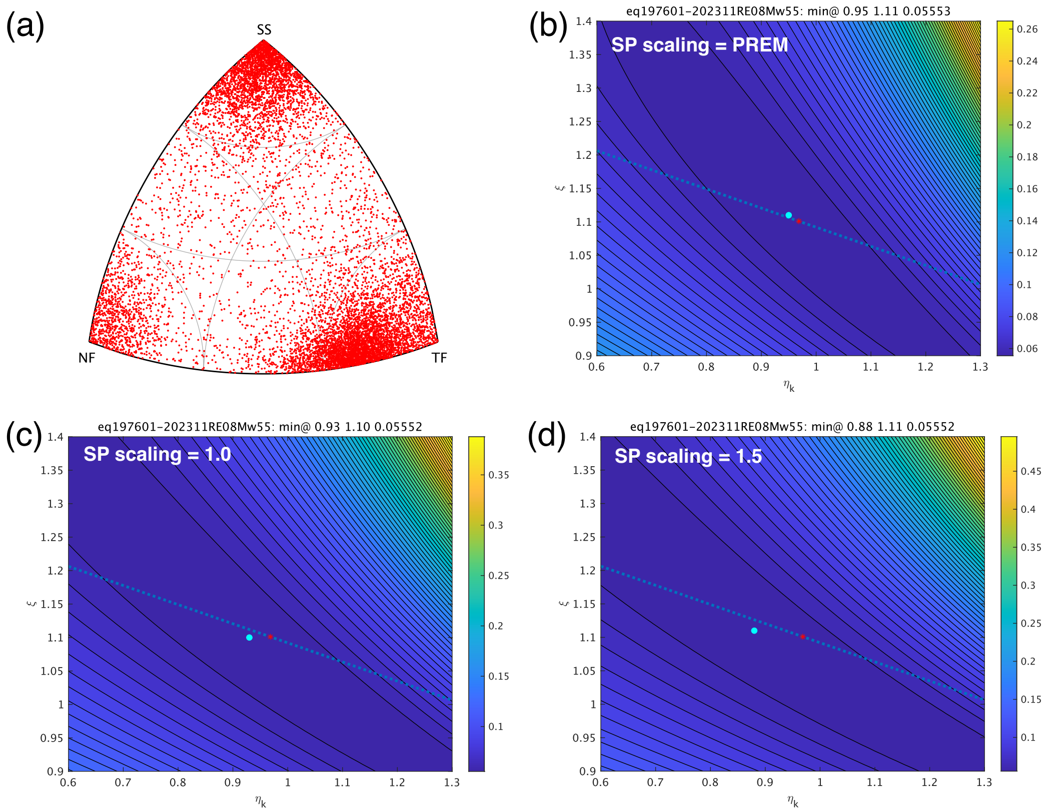

Figure 6: Grid-search results for the entire GCMT dataset. (a) The fault-type diagram showing the distribution of the CMT solutions. The concentration of points near the tree corners may reflect plate tectonic origin of earthquakes. The high density area along the lower edge of the diagram near the thrust fault (TF) corner may be due to the low-angle thrust faults sub-parallel to the subducting oceanic plate interface. (b-d) The same as in Figure 5 but for the GCMT dataset with different S-P s. (The point in cyan color gives the minimum const-function location, and the red asterisk denotes the PREM sub-Moho point as a reference.) The increase of the scaling coefficient appear to shit the location of the minimum valley away from the PREM sib-Moho model. Note that the minimum misfit values indicated at the top-right of each plot are almost equal to each other indicating the lack of resolution for the S-P scaling.

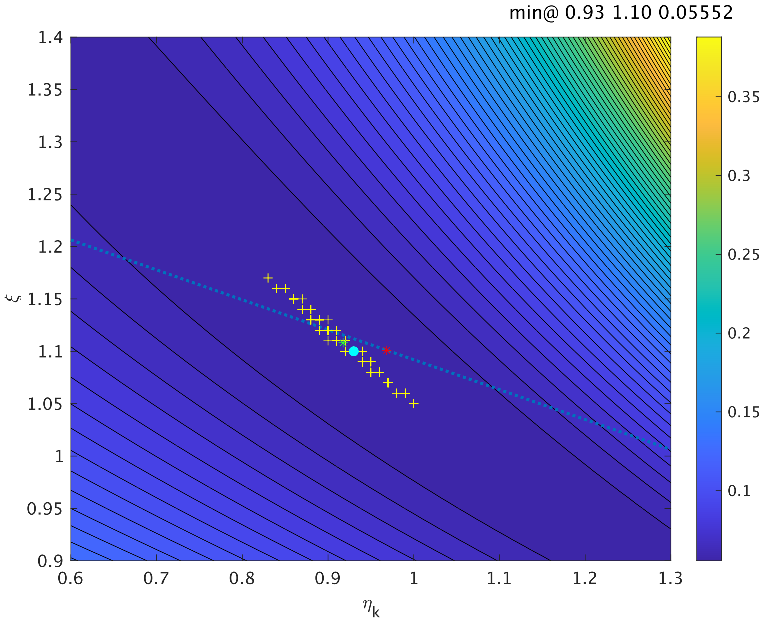

Figure 7: Bootstrap error estimate. The same as in Figure 6b, but the results of 500 bootstrap resampling are shown by yellow plus marks. The point in cyan color gives the minimum const-function location, and the red asterisk denotes the PREM sub-Moho point as a reference. The green asterisk indicates the boot strap average. Note that the resampling minimum points are mostly scattered along the minimum valley of the misfit map, indicating the lack of the resolution along the valley.

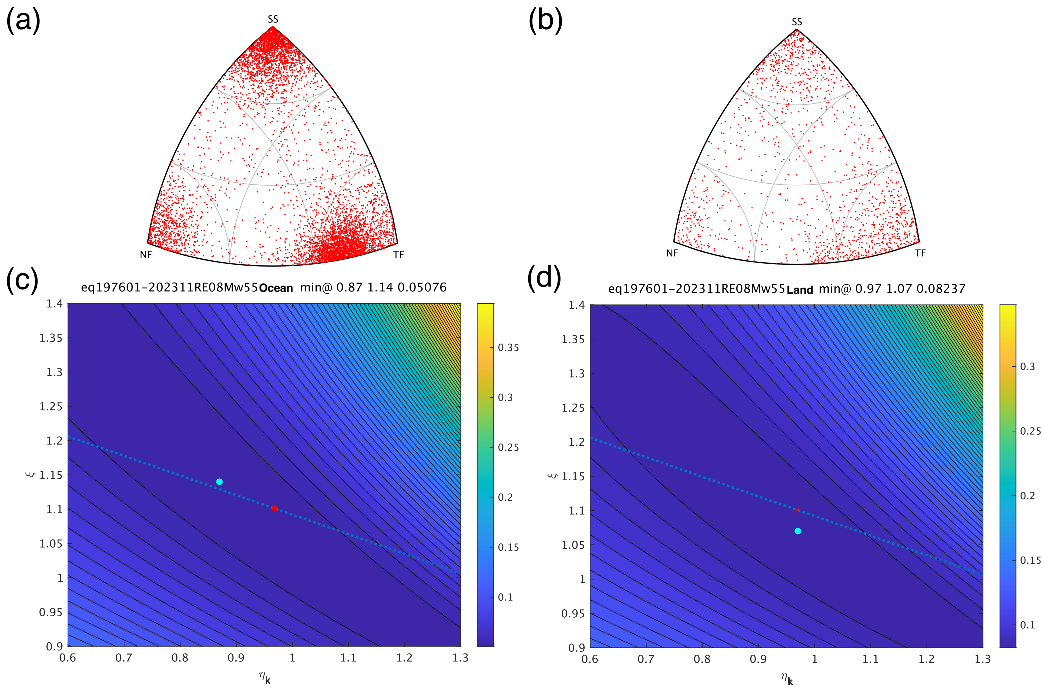

Figure 8: Ocean vs Continent: Similar plots as in Figure 6 but for the datasets for earthquakes in (a,c) oceanic and (b,d) continental regions with S-P scaling=1.

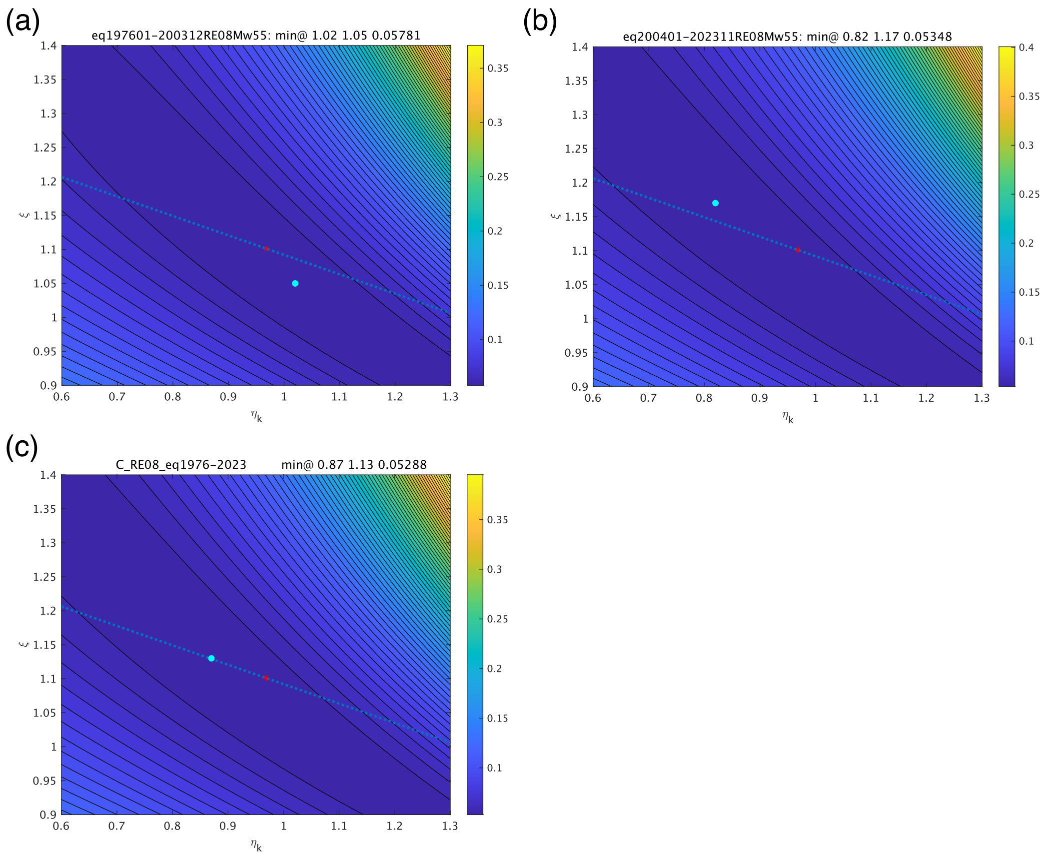

Figure 9: Time lapse: Similar plots as in Figure 8(c),(d) but for the datasets for earthquakes occurring in (a) 1976-2003, (b) 2004-2023.11, and (c) for the combined data-types (C) in 1976-2023.11 , all with S-P scaling=1.

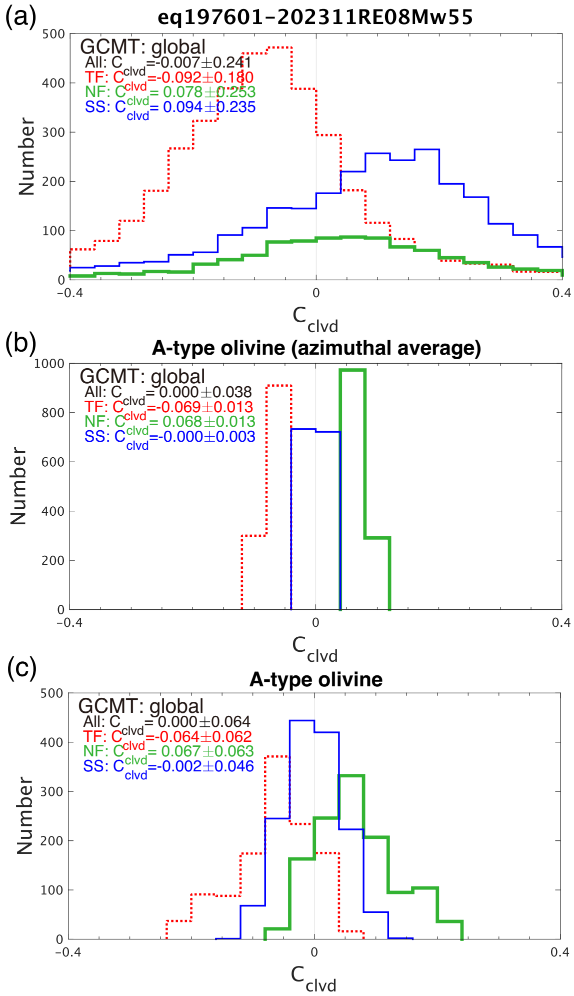

Figure 10: Histograms showing the distribution of the NDCs of (a) the quality controlled GCMT data used in the analysis, (b) synthetic MTs for 10000 randomly generated faults in an anisotropic source region equivalent of the azimuthally averaged A-type olivine (i.e., VTI) fabric, and (c) those for A-type olivine (assume vertical b-axis). Red (dotted), green (thick) and blue (thin) colors (lines) correspond to TF, RF, and SS. Note that the introduction of more realistic (e.g., azimuthal) anisotropy increases the spread of the NDCs.

Characterizing Lithospheric Transverse Isotropy using Moment Tensors
- On the origin of the Non-double Couple Components of GCMT solutions -

Hitoshi Kawakatsu[1,2] (e-mail: hitosi@eri.u-tokyo.ac.jp)

[1]Earthquake Research Institute, The University of Tokyo, Japan
[2]Institute of Earth Sciences, Academia Sinica, Taiwan

Supplemental Material

Representation of VTI

In a VTI or equivalently radial anisotropy system, horizontally and vertically propagating P-waves have phase velocities of

$$\alpha_H = \sqrt{A/\rho}, \quad and \quad \alpha_V = \sqrt{C/\rho},$$

respectively, where ρ gives the density, and A and C denote Love's elastic constants. As for shear waves, with Love's constants L and N, horizontally and vertically polarized *horizontally propagating S-waves* respectively have phase velocities of

$$\beta_H = \sqrt{N/\rho}, \quad and \quad \beta_V = \sqrt{L/\rho},$$

and *vertically propagating S-waves* also have a phase velocity of β_V ($cf.$ Figure 1 of Kawakatsu (2016a)). So for these horizontally or vertically traveling bodywaves, the ratios of Love's elastic constants define the degree of radial anisotropy,

$$\phi^{-1} = A/C = \alpha_H^2/\alpha_V^2, \quad and \quad \xi = N/L = \beta_H^2/\beta_V^2,$$

for the P-wave and the S-wave, respectively. As for the P-wave anisotropy index, we specifically use ϕ^{-1} (instead of ϕ), because for many of realistic cases, the strength of anisotropy for P and S is positively correlated. For other intermediate direction bodywaves, the Love's fifth elastic constant, F, affects the incidence angle dependence of quasi-P and quasi-SV waves via η_κ,

$$\eta_\kappa \;=\; \frac{(F+L)}{(A-L)^{1/2}(C-L)^{1/2}}$$

(Kawakatsu, 2016a).

References

Kawakatsu, H., 2016a. A new fifth parameter for transverse isotropy. Geophys. J. Int. 204, 682–685. doi:10.1093/gji/ggv479.

Kustowski, B., Ekstrom, G., Dziewonski, A.M., 2008. Anisotropic shear-wave velocity structure of the Earth's mantle: A global model. Earth Planet. Sci. Lett. 113, B06306. doi:10.1029/2007JB005169.

Data source	Total number	Thrust			Normal			Strike slip		
		N	μ	σ	N	μ	σ	N	μ	σ
$\mathrm{GCMT}^{\star}_{-B}$	2434	990	-0.143	0.192	172	0.132	0.284	739	0.085	0.244
$\mathrm{GCMT}^{\star}_{-C}$	1537	578	-0.060	0.164	159	0.071	0.252	441	0.056	0.243

Table S1: Statistics of NDCs via $C_{CLVD}(= 2\epsilon)$ similar to Table 2. $\mathrm{GCMT}^{\star}_{-B}$ and $\mathrm{GCMT}^{\star}_{-C}$ correspond to bodywave only and surface wave combined solutions for pre-2004 data used for Figure S7.

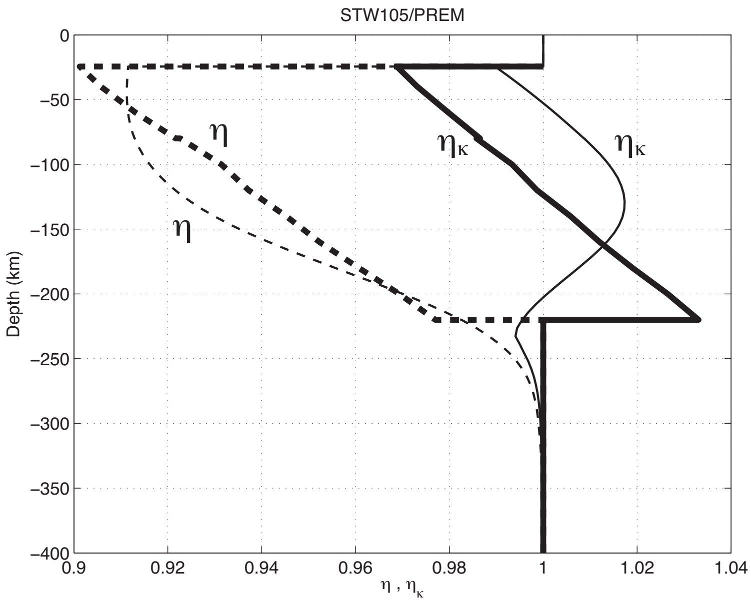

Figure S1: Figure after Kawakatsu (2016a). The thick solid and broken lines respectively show η_κ and η of PREM as a function of the depth that are compared with those of Kustowski et al. (2008).

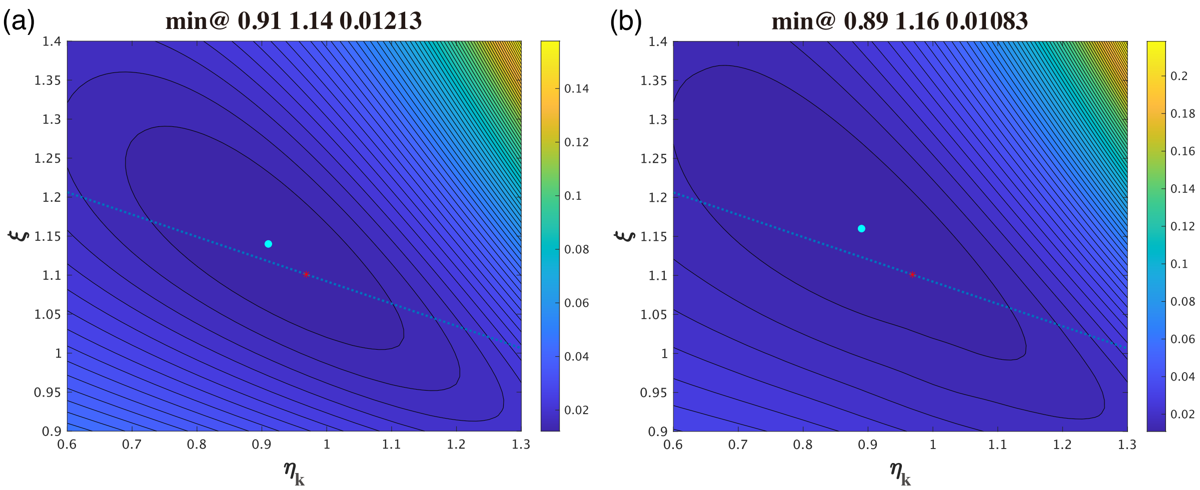

Figure S2: More results of resolution tests. (a) The same as Figure 5c, but for the synthetic moment tensor data with a random noise of 10% added. The point in cyan color gives the minimum const-function location, and the red asterisk denotes the PREM sub-Moho point as a reference. (b) The same as (a), but for the cost function that is $2\Gamma_m$ in (17).

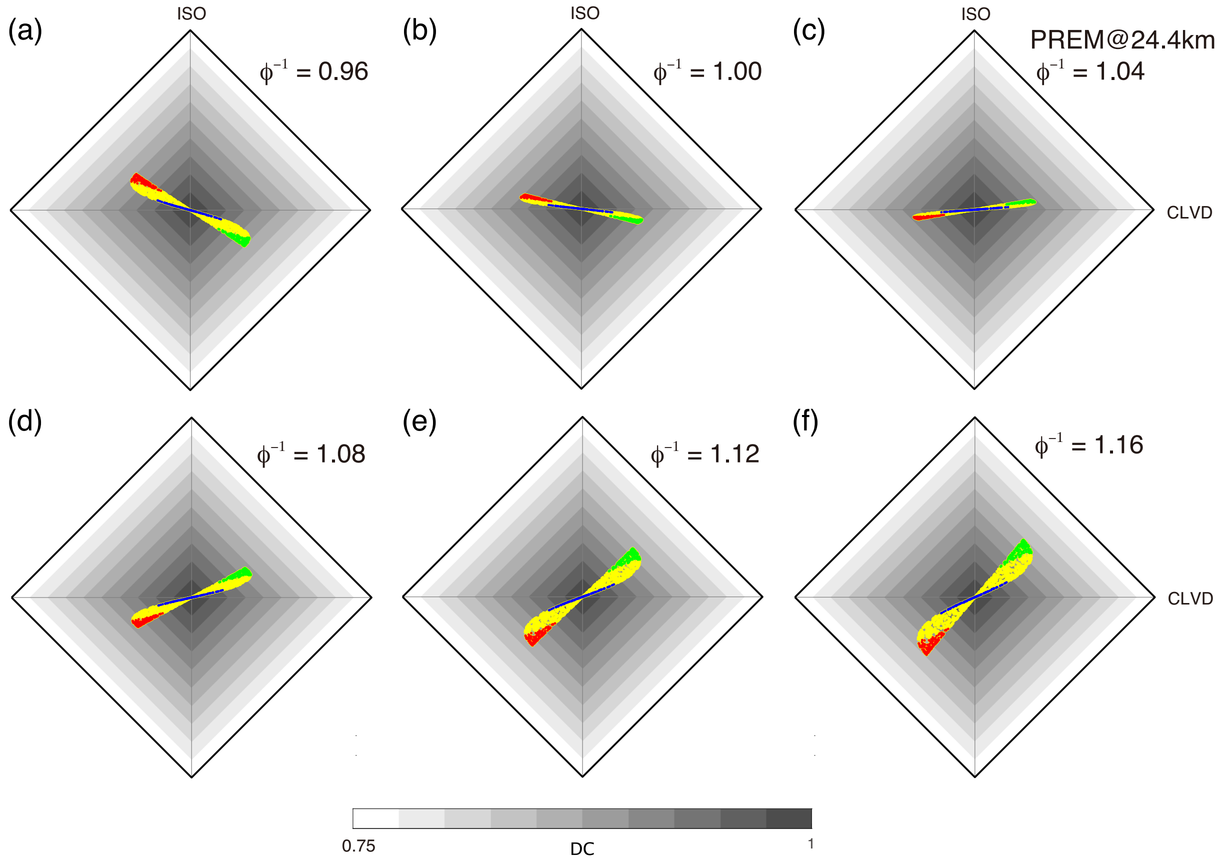

Figure S3: The same as Figure 2b, but for different VTI models with varying ϕ^{-1} value: (a) ϕ^{-1}=0.96, (b) 1.00, (c) PREM sub-Moho (1.04), (d) 1.08, (e) 1.12, (f) 1.16

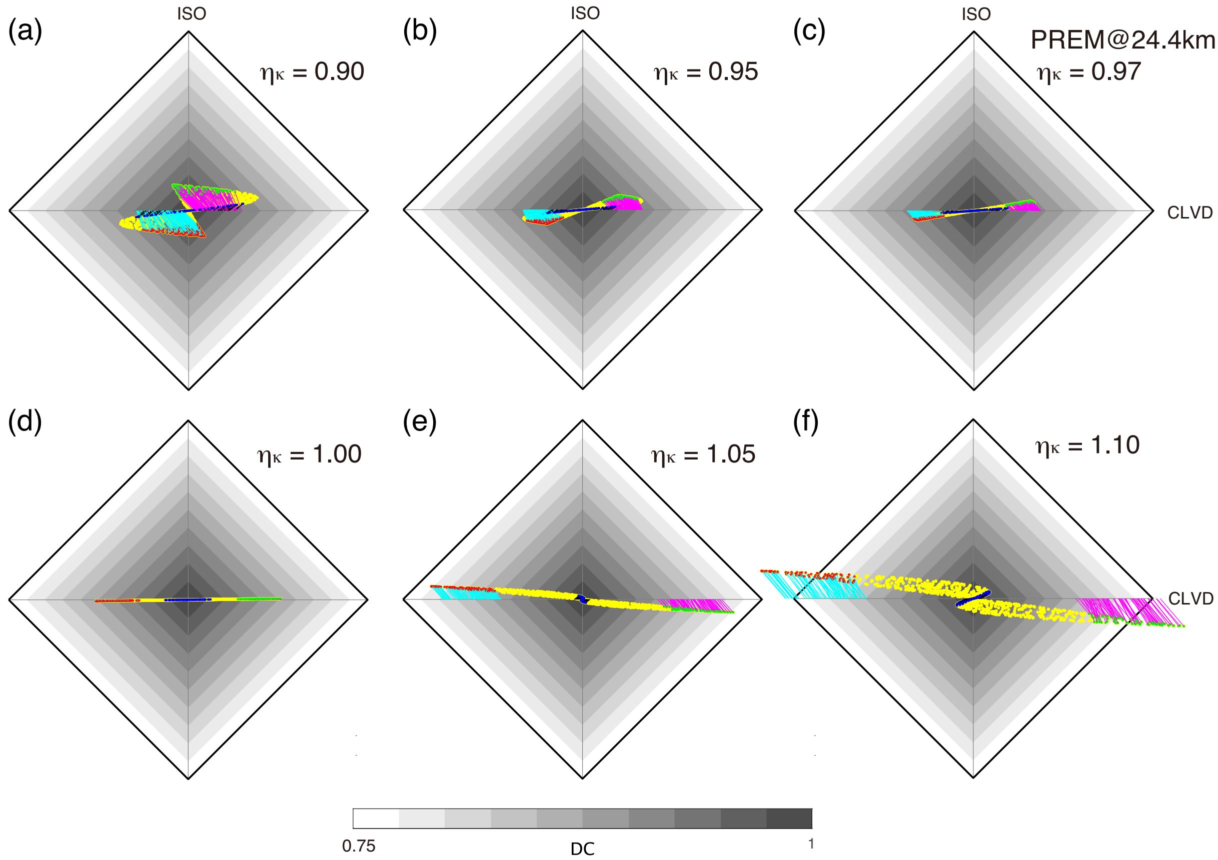

Figure S4: The same as Figure 2c, but for varying η_κ

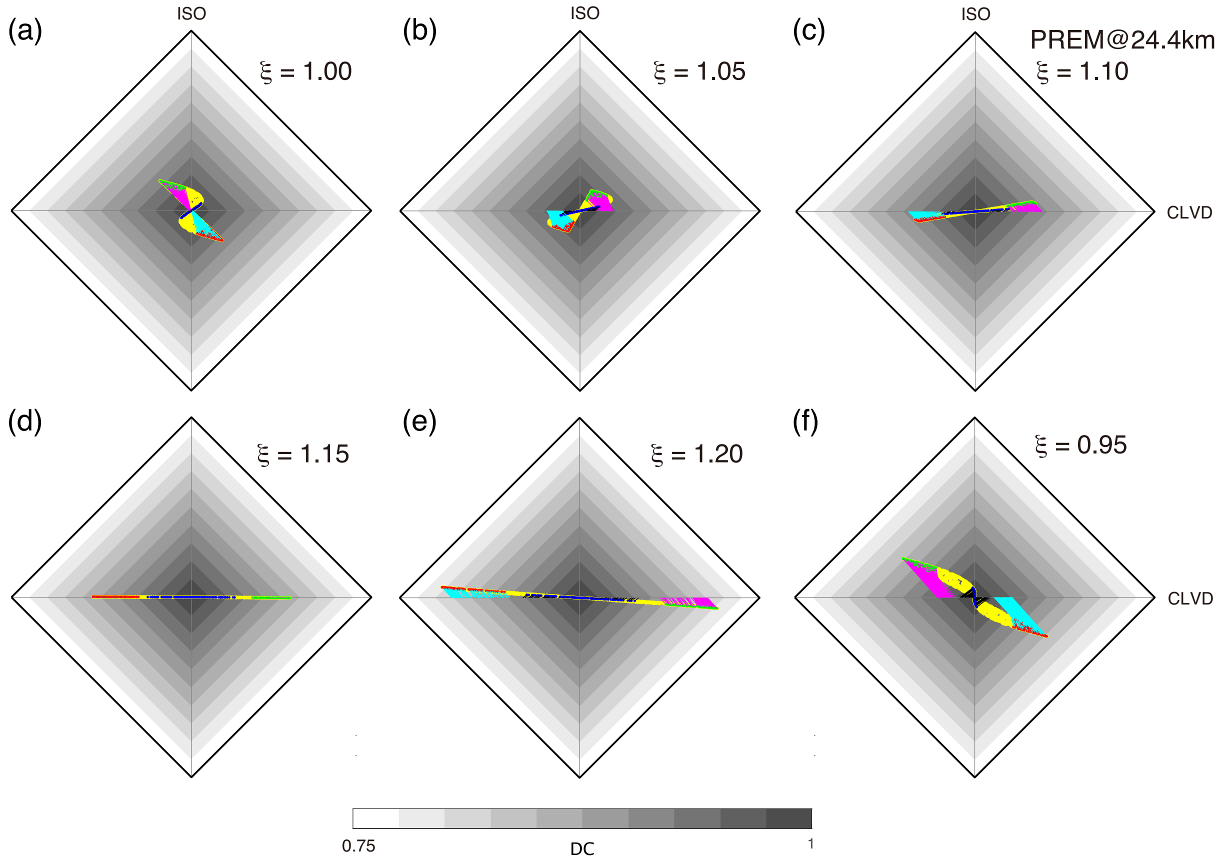

Figure S5: The same as Figure S4, but for varying ξ

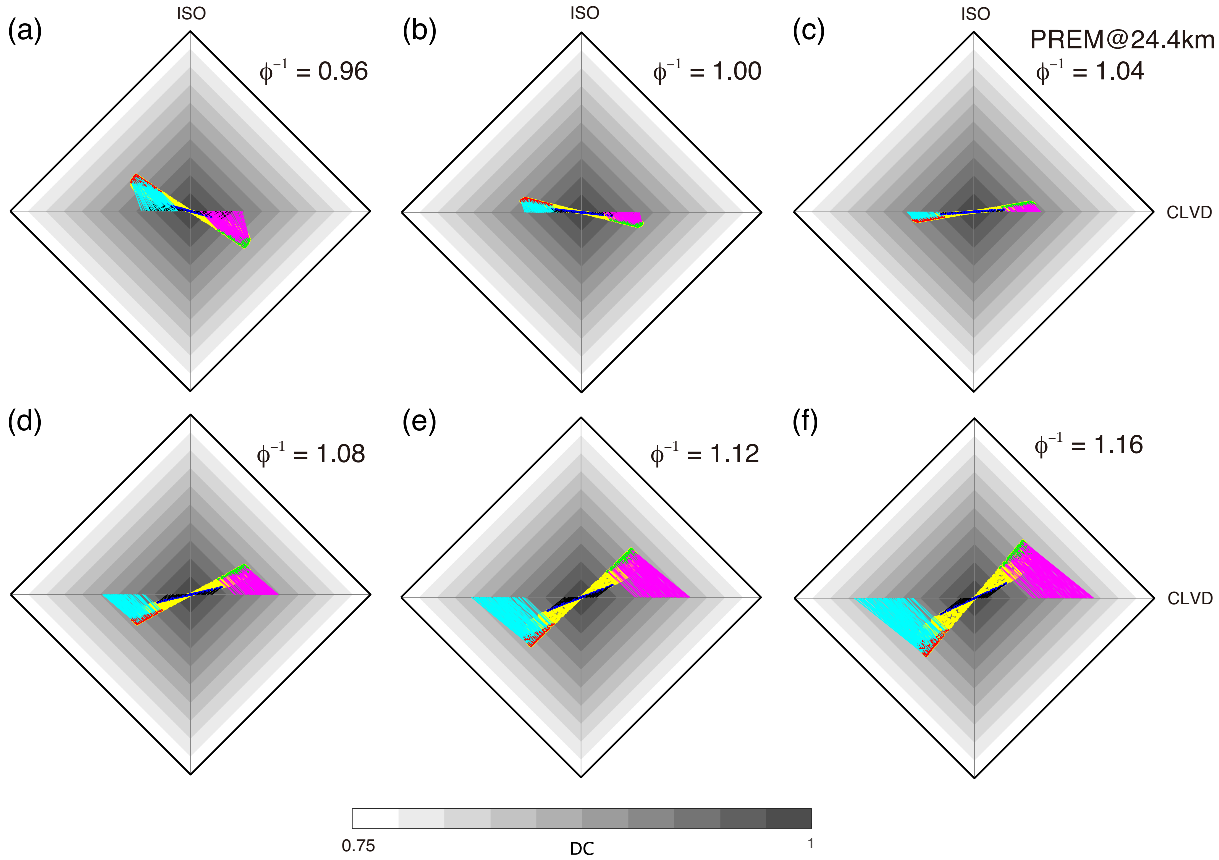

Figure S6: The same as Figure S4, but for varying ϕ^{-1}

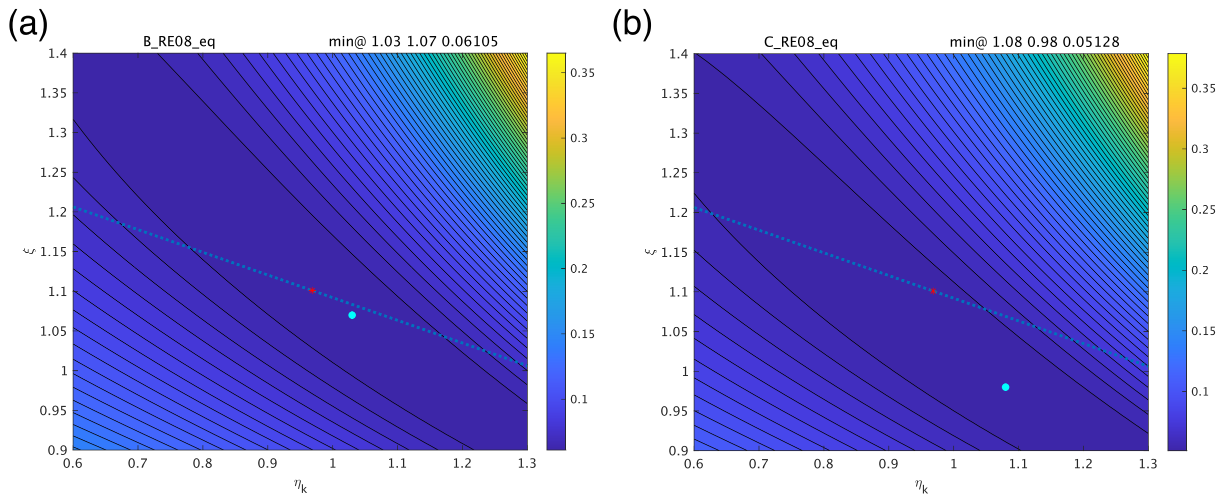

Figure S7: Data-type dependence: Similar plots as in Figure 9 but for earthquakes occurring in 1976-2003 with (a) bodywave only and (b) surface wave combined solutions.